Pathways and supply of dissolved iron in the Amundsen Sea (Antarctica)

P. St-Laurent[1], P.L. Yager[2], R.M. Sherrell[3], S.E. Stammerjohn[4] and M.S. Dinniman[1]

[1]Center for Coastal Physical Oceanography, Old Dominion University, Norfolk, VA
[2]Department of Marine Sciences, University of Georgia, Athens, GA
[3]Department of Marine and Coastal Sciences and Earth and Planetary Sciences, Rutgers University, New Brunswick, NJ
[4]Institute of Arctic and Alpine Research, University of Colorado, Boulder, CO

Key Points:

- Four sources of dissolved iron are implemented in a numerical sea ice-ice shelf-ocean model
- Modeled dissolved iron distributions reproduce observed enhanced concentrations near ice shelf fronts
- Ice shelf melting contributes directly and indirectly to the supply and delivery of dissolved iron

Corresponding author: Pierre St-Laurent, `pstlaure@odu.edu`

Abstract

Numerous coastal polynyas fringe the Antarctic continent and strongly influence the productivity of Antarctic shelf systems. Of the 46 Antarctic coastal polynyas documented in a recent study, the Amundsen Sea Polynya (ASP) stands out as having the highest net primary production per unit area. Incubation experiments suggest that this productivity is partly controlled by the availability of dissolved iron (dFe). As a first step toward understanding the iron supply of the ASP, we introduce four plausible sources of dFe and simulate their steady spatial distribution using conservative numerical tracers. The modeled distributions replicate important features from observations including dFe maxima at the bottom of deep troughs and enhanced concentrations near the ice shelf fronts. A perturbation experiment with an idealized drawdown mimicking summertime biological uptake and subsequent resupply suggests that glacial meltwater and sediment-derived dFe are the main contributors to the pre-bloom dFe inventory in the top 100 m of the ASP. The sediment-derived dFe depends strongly on the buoyancy-driven overturning circulation associated with the melting ice shelves (the 'meltwater pump') to add dFe to the upper 300 m of the water column. The results support the view that ice shelf melting plays an important direct and indirect role in the dFe supply and delivery to polynyas such as the ASP.

1 Introduction

The Antarctic continental shelves feature numerous coastal 'polynyas' fringing the continent [*Nihashi and Ohshima*, 2015]. These are openings in the sea ice along the coast and, in the case of Antarctica, are typically caused by seaward-directed winds [latent heat polynyas, *Morales Maqueda et al.*, 2004]. The polynyas favor primary production by providing light in areas that are otherwise covered by sea ice. During the summer season, the melting of sea ice also provides vertical stratification that prevents primary producers from being mixed far below the euphotic zone.

Of the 46 Antarctic coastal polynyas documented by *Arrigo et al.* [2015], the Amundsen Sea Polynya (ASP) stands out by its high Net Primary Production (NPP) per unit area (105.4 g-C m^{-2} yr^{-1}, 16% greater than the runner-up, the Ross Sea Polynya). Although the causes of this high productivity may be complex, it has been suggested that the availability of dissolved iron (dFe, a micro-nutrient essential for algal production) plays a substantial role in the productivity of the ASP [*Arrigo et al.*, 2015; *Yager et al.*, 2012; *Sherrell et al.*, 2015]. The incubation experiments of *Alderkamp et al.* [2015] provide direct observational support for a primary production that would be stressed by low iron concentrations during the months of December and January (austral summer).

The most comprehensive dFe dataset from the ASP was collected in December 2010 and January 2011 during the Amundsen Sea Polynya International Research Expedition [ASPIRE, *Yager et al.*, 2012]. The dataset consists of 20 vertical profiles covering in most cases the surface to the bottom [*Sherrell et al.*, 2015]. The profiles exhibit relatively uniform concentrations of 0.3–0.4 nM between 150 m and 300 m and rapidly increasing concentrations near the sea floor (Figure 3a of *Sherrell et al.* [2015]). The relatively uniform concentrations away from the sea floor are associated with the two main water masses on the continental shelf, Circumpolar Deep Water (CDW) and Winter Water (WW), characterized by similar dFe con-

centrations of 0.37 nM and 0.3 nM respectively [*Yager et al.*, 2016; *Sherrell et al.*, 2015]. The former intrudes over the continental shelf within the large glacial troughs and occupies the water column below ~ 350 m [e.g., *Jacobs et al.*, 2012]. Winter Water occupies the upper part of the water column and is substantially cooler and fresher because of surface exchanges with the atmosphere and sea ice. Winter Water is temporarily layered between CDW and warm Antarctic Surface Water (AASW) during the summer period.

The rapid increase in dFe concentrations below 300 m is not well understood. *Sherrell et al.* [2015] suggested that the increase could represent inputs from the continental shelf terrigenous sediments to the near-bottom waters of the deep troughs. This deep dFe could also represent the remineralization of organic-bound pFe on or near the sediment surface. In general, deeper stations show higher bottom concentrations while shallow stations (positioned on ridges) show smaller increases near the bottom. It remains unclear whether this feature represents: (1) spatial variations in the magnitude of the iron flux from the sediments, (2) lateral dispersion and dilution from the bathymetric highs, (3) vertical mixing caused by physical processes at the surface and redistributing dFe over the entire water column at shallower stations, or (4) spatial variations in the sinking flux of particulate organic matter and its accumulation over time.

Dissolved iron concentrations typically decrease from 150 m to the surface during the summer [Figure 3e of *Sherrell et al.*, 2015] which is attributed to biogeochemical removal processes [scavenging, biological uptake; *Bruland et al.*, 2014]. No obvious dFe enrichment was observed at the surface of stations with low-salinity surface water. The lack of surface enrichment suggests that sea ice melt was not a substantial input of dFe or that the enrichment was followed by a rapid uptake by phytoplankton, prior to the sampling time. Another factor contributing to the lack of surface enrichment would be that the ASP mostly produces and exports sea ice [e.g., *Nihashi and Ohshima*, 2015].

The observed summertime dFe distributions are complex: they represent the result of multiple iron inputs combining over different spatial and temporal scales, and they are modified by biogeochemical processes. In this study, we simplify this formidable problem by focusing on four iron sources and by simulating their distribution in absence of biogeochemical processes. Our approach is based on an existing high-resolution sea ice-ice shelf-ocean coupled model [*St-Laurent et al.*, 2015] that we use to illustrate the pathways of the different iron sources and their distribution inside the Amundsen Sea. Although the picture obtained in the end is necessarily incomplete as the model omits iron removal processes, it represents a significant step toward understanding the iron supply and its potentially important role in the productivity and interannual variability of the ASP.

The study is structured as follows. The next section describes our model approach and includes extensive model–data comparisons to highlight the model strengths as well as its weaknesses and purposeful omissions. The third section illustrates the pathways of the different iron sources and their distribution inside the Amundsen Sea. The simulated distributions provide information on the relative abundance of each iron sources while their sum is compared with *in situ* observations. Perturbation experiments are then used to highlight the role of certain physical mechanisms in the modeled distributions. Finally, we discuss the lessons

learned from the idealized experiments and their implications for the biological production of the ASP.

2 Method

2.1 Numerical model of the Amundsen Sea

The study relies on an existing numerical model of the Amundsen Sea [*St-Laurent et al.*, 2015] based on the Regional Ocean Modelling System [ROMS, *Shchepetkin and McWilliams*, 2005]. It includes dynamic-thermodynamic sea ice [*Budgell*, 2005; *Mellor and Kantha*, 1989] and static ice shelves thermodynamically-coupled to the ocean with transfer coefficients that are a function of the friction velocity [*Dinniman et al.*, 2011; *Holland and Jenkins*, 1999]. The model domain (see Figure 1) covers the entire Amundsen Sea continental shelf with a uniform horizontal spacing of 1.5 km to properly resolve the small ice shelf cavities as well as mesoscale processes. The model is forced with daily averaged winds from the Antarctic Mesoscale Prediction System [AMPS, *Powers et al.*, 2012]. Atmospheric fields other than winds and surface air temperature are from ERA-Interim [*Dee et al.*, 2011] with monthly frequency. The model uses bulk formulas to calculate surface fluxes from the simulated ocean conditions and the prescribed surface atmospheric conditions [COARE 3.0, *Fairall et al.*, 2003]. No tidal forcing is applied to avoid aliasing by the daily model outputs. The lateral ocean boundary conditions for salinity and temperature are from a monthly climatology assembled from 5 day state estimates [Southern Ocean State Estimate, SOSE, *Mazloff et al.*, 2010] for the period Jan. 1, 2008 to Dec. 31, 2010.

Several improvements were made to the model since the study of *St-Laurent et al.* [2015]. The model bathymetry and ice shelf draft were updated with the datasets of *Millan et al.* [2017] and *Schaffer et al.* [2016]. The shape of the Thwaites Fast-ice Tongue (TFT, Figure 1) was revised to be closer to the configuration visible in satellite images [*Scambos et al.*, 2017] around Dec. 2010 (i.e. the period of the ASPIRE sampling). As in *St-Laurent et al.* [2015], the TFT is assumed static and has a fixed thickness (1 m) allowing the ocean to circulate underneath it. The exceptionally large iceberg B-22, present in the Amundsen Sea during the same period (Figure 1), was added as a static obstacle extending from the surface to the sea floor (i.e., similar to an island). Finally, the effect of the numerous smaller icebergs grounded between Crosson ice shelf and iceberg B-22 is acknowledged by simply prescribing static sea ice every other grid point along a line between Bear Peninsula and the TFT (see Figure 1). This 'permeable barrier' slows down the northward flux of sea ice and produces sea ice distributions that are consistent with satellite images [*Scambos et al.*, 2017] without having to represent each small individual icebergs. As for the TFT, the barrier of static sea ice has a fixed thickness (1 m) and the ocean is free to circulate underneath it.

The model biharmonic horizontal viscosity was replaced with a very low Laplacian viscosity ($0.1\,\mathrm{m^2\ s^{-1}}$). For the tracers, the horizontal Laplacian diffusivity was decreased to $0.1\,\mathrm{m^2\ s^{-1}}$. These viscosity/diffusivity coefficients represent the lowest values that guarantee spatially smooth fields. The monthly surface air temperature from ERA-Interim [*Dee et al.*, 2011] was replaced by monthly fields of higher spatial resolution from the Antarctic Mesoscale Prediction System [AMPS, *Powers et al.*, 2012]. Finally, the sea ice concentration at the model open boundaries is now from SSM/I [*Comiso*, 1999] and includes interannual variabil-

ity for the entire simulation period. As in *St-Laurent et al.* [2015], all model simulations cover the period Jan. 1, 2006 to Dec. 31, 2013.

2.2 Model–data comparisons

We present model–data comparisons for basal melt rates, salinity and temperature profiles, glacial meltwater and sea ice concentration. The model generally reproduces the large differences in the basal melt rates of the seven ice shelves in the Amundsen Sea (Figure 2). The model biases are lower than or comparable to other models of this area [*Jourdain et al.*, 2017, their Table B1]. The main discrepancy is a high bias for the melt rate of the Getz ice shelf. This bias was already apparent in *St-Laurent et al.* [2015] and attributed to a high temperature bias at the western open boundary.

Alongside the dFe data set, the ASPIRE dataset provides 65 profiles of salinity and potential temperature concentrated within the ASP [*Randall-Goodwin et al.*, 2015] and collected by a second (non-trace metal clean) CTD rosette package during the period of mid Dec. 2010 to early Jan. 2011. The profiles are compared with the corresponding model fields averaged over the month of Dec. 2010 (to minimize the signature of individual eddies) and sampled at the closest model grid point. The model correctly captures the top-to-bottom changes in both salinity and temperature (Figure 2). The main discrepancies correspond to a $+0.1$ psu bias in salinity (from surface to bottom), a $+0.2°$C bias at the surface, a $-0.25°$C bias around 400 m, and a $+0.1°$C bias at 800 m. The salinity bias could be caused by neglecting glacial calving and iceberg melt or by a bias in the open boundary conditions. The temperature biases are fairly small with no obvious causes.

The modeled glacial meltwater (see Section 2.3 on how it is calculated) is evaluated with two different datasets: one from noble gases [neon, *Kim et al.*, 2016b] and the other one from a combination of salinity, potential temperature and dissolved oxygen [S, θ, dO; e.g., *Randall-Goodwin et al.*, 2015]. Each approach has limitations. Neon data are affected by gas loss near the surface, which would cause an underestimation of glacial meltwater concentrations in the surface layers [*Kim et al.*, 2016b; *Hohmann et al.*, 2002]. Similarly, surface fluxes and biological activity render S, θ, dO non-conservative in the upper layers and lead to diverging estimates of glacial meltwater [*Randall-Goodwin et al.*, 2015]. Variability in the characteristics of the source water masses also affect the meltwater concentrations [*Biddle et al.*, 2017]. Nevertheless, both approaches are found to be consistent in the deeper layers that are unaffected by surface fluxes [i.e. below ~ 300 m, *Kim et al.*, 2016b, their Figure 5].

For our model–data comparison, we separately examine the vertical distribution of glacial meltwater (based on neon) and the horizontal distribution (based on S, θ, dO). The neon dataset is expected to be more accurate in the upper layers (hence its use for the vertical distribution) while the S, θ, dO dataset covers a larger horizontal area. Regarding the timing of the sampling, the S, θ, dO data were collected during ASPIRE (mid Dec. 2010 to early Jan. 2011), while the neon data were collected in Jan. 2011 and Feb. 2012. The modeled glacial meltwater distribution represents an average over the month of Dec. 2010 and was preceded by a 13-year spin-up to eliminate trends in the tracer inventory. Hereafter we refer to such tracer fields as being 'stationary'. The modeled concentrations show relatively small (seasonal) variations after this spin-up period and thus the differences in temporal coverage (Dec. 2010

versus Jan. 2011 or Feb. 2012) have a minor influence on the outcome of the model–data comparison.

For the vertical distribution of glacial meltwater, the observations and model show concentrations in the range 0–17 ppt (Figure 3). The largest values are observed near the ice shelf front and particularly on the western side of the Dotson ice shelf (Station 27). The modeled concentrations are of reasonable magnitude but their vertical distribution is biased: modeled values are systematically lower (higher) than observed below (above) 500 m. The bias suggests that the modeled vertical mixing is underestimated inside the ice shelf cavities and/or on the continental shelf, leading to profiles that are surface-intensified compared to observations (i.e., the modeled glacial meltwater outflow would be too buoyant). The highest modeled concentrations are found at Station 25 (Getz Ice Shelf) but modeled concentrations remain high all along the front of the Dotson/Getz ice shelves. Both the neon data and the model suggest that glacial meltwater extends far northward in direction of the shelf break (Station 7, observed concentrations of 4–5 ppt). However, the modeled concentrations have a high bias of +5 ppt above 200 m at this station. It suggests that the model exaggerates the northward spread of the glacial meltwater (at least in this depth range).

The horizontal distribution of glacial meltwater is examined along a deep density surface (1027.56 kg m^{-3}, approximately 450 m) to limit the influence of surface fluxes. The observations along this density surface show values in the range 5–9 ppt (Figure 4). Values are highest at the front of the Dotson ice shelf ($\sim$ 9 ppt), average within the ASP ($\sim$ 7 ppt), and lowest in front of the Getz ice shelf ($\sim$ 5 ppt). The magnitude of the modeled distribution is reasonable within the polynya with concentrations around 7 ppt but the model underestimates the value at certain stations. Observations and model show values $\sim$6 ppt at the shelf break but modeled concentrations rapidly decrease beyond this point. The model appears to underestimate meltwater concentrations within the outflow from the Dotson ice shelf cavity (-1.5 ppt bias) and to overestimate concentrations in front of Getz ice shelf ($+3$ ppt bias). Note that the model overestimates the basal melt of the latter (Figure 2).

The model–data comparison for sea ice concentration (Figure 5) is based on years 2010–2011 of the high-resolution AMSR-E dataset [12.5 km resolution, *Cavalieri et al.*, 2014]. This particular period corresponds to the ASPIRE cruise and matches the TFT configuration prescribed in the model (see Section 2.1; note also that AMSR-E became unavailable after Sep. 2011). The model captures the progression of the polynya from fully closed in July 2010 to a full extension in Feb. 2011 and then mostly closed in June 2011. The model tends to overestimate (underestimate) the sea ice concentration in the ASP over the months preceding (following) Feb. 2011. The model also underestimates the extent of Pine Island Polynya (northward of PIG; Figure 1) throughout the year. These model biases are likely related to the model wind forcing that influences both sea ice advection (opening of polynya) and sea ice production (closing of polynya). The lack of interactive coupling between the atmosphere and the sea ice-ocean model may also contribute to these biases.

2.3 Modeling four sources of dissolved iron

The goal of this study is to simulate the distribution of dFe from four sources in absence of biogeochemical processes and to compare the results with observations collected during

ASPIRE. These four sources of dFe are selected for their known importance in the Amundsen Sea or in other Antarctic shelf environments: 1) CDW originating from the shelf break and intruding over the shelf [e.g., *McGillicuddy et al.*, 2015], 2) glacial meltwater [gmw, *Gerringa et al.*, 2012; *De'Ath et al.*, 2014], 3) deep sediments on the continental shelf [*Sherrell et al.*, 2015; *Marsay et al.*, 2014], and 4) sea ice [sice, *Lannuzel et al.*, 2016]. Here we use 'sediments' to refer to the large dFe inventory near the sea floor with the understanding that the details of the mechanisms leading to the high concentrations remain undetermined (see Section 1).

The basic assumption behind our idealized experiment is that observed dFe distributions would be supplied by a combination of:

$$dFe_{observed} = dFe_{sediments} + dFe_{CDW} + dFe_{gmw} + dFe_{sice}, \tag{1}$$

where the term $dFe_{sediments}$ should be interpreted as 'the dissolved iron concentration at a given point in time and space that originated from deep sediments', and so on for the other sources. The four sources and the assumptions behind them are described in further detail in the next sections. Other potential sources such as aeolian deposition and hydrothermal vents are justifiably neglected [*Sherrell et al.*, 2015; *Gerringa et al.*, 2012]. The biogeochemical processes neglected in this experiment primarily act to remove dFe from the water column (e.g., biological uptake, iron scavenging) and thus represent a sink of dissolved iron (one exception being the recycling of particulate organic matter).

The idealized experiment fulfills three objectives. The first one is to determine the pathways of the four dFe sources throughout the Amundsen Sea. For example, what happens to glacial meltwater (and the dFe associated with it) after it leaves the ice shelf cavities is very difficult to determine from observations alone. The second objective is to quantify the relative contribution of each of the dFe sources to the total dFe inventory. This is achieved by integrating the individual dFe sources over multiple years (as in real life) until they reach a stationary concentration that can be compared to observations, again assuming simplistically that biogeochemical removal does not occur and that dFe can only be removed through advection out of the domain. The third objective, intended to address this obvious simplification that dFe acts as a conservative tracer, is to represent an idealized 'biological drawdown' in the upper 100 m and to determine how quickly the dFe inventory of the upper 100 m can be replenished by advection and mixing of the four iron sources after the summer drawdown.

The dFe concentrations associated with gmw, sediments and CDW are calculated using an Eulerian tracer [e.g., *Mack et al.*, 2017]. These tracers are assumed conservative and evolve over time according to the modeled oceanic circulation and diffusion. The tracers are independent of each other and they do not affect the model physics (passive tracers). The concentration of each tracer is expressed in parts per thousand (ppt) and is converted into a dFe concentration by attributing a constant end-member to each source (see Sections 2.3.1, 2.3.2, 2.3.3). The fourth dFe source (sea ice, Section 2.3.4) is simply calculated from the summer sea ice meltwater flux.

2.3.1 Circumpolar Deep Water

The first Eulerian tracer represents CDW at the shelf break. This water mass floods the continental shelf of the Amundsen Sea and occupies the bulk of the water column in the

eastern Amundsen Sea [e.g., *Jacobs et al.*, 2012]. Following *Sherrell et al.* [2015], the CDW at the shelf break is defined in the model with a potential temperature criterion $\theta \geq 0.7°C$ and attributed an end-member dFe concentration of 0.37 nM. The initial condition (Jan. 1, 2006) has no CDW on the continental shelf ($c = 0$ ppt) and 'pure' CDW ($c = 1000$ ppt) in areas off the continental shelf meeting $\theta \geq 0.7°C$. The same temperature criterion is used to prescribe the tracer concentration at the model open boundaries (see Figure 1 for their location). With this choice of open boundary conditions, the water on the continental shelf of the model is a mixture of: (1) CDW originating from the shelf break, and (2) non-CDW water ($\theta < 0.7°C$) originating from outside the model domain. The contribution of the latter to the modeled dFe inventory is neglected for simplicity (a proper treatment of which would require seasonal variations representing biological uptake).

Water masses such as CDW are normally affected by surface fluxes (notably during winter) that modify their physical characteristics (salinity, temperature) and ultimately transform them into Winter Water and AASW. On the other hand, such physical transformations are not expected to influence the dFe concentration of the water mass (which is our main interest in this study). We thus consider the CDW tracer as conservative and neglect the physical transformation into Winter Water.

2.3.2 Glacial ice

The second Eulerian tracer represents dFe contained in glacial meltwater. Dissolved iron concentrations associated with glacial meltwater are thought to be substantial [*Gerringa et al.*, 2012; *De'Ath et al.*, 2014] and may originate from aeolian material deposited over the continent and integrated into the ice sheet over its history, or from scouring of the ice sheet over the continental bedrock resulting in high iron content near the base of the glacier. In the case of this study, we only simulate the glacial meltwater produced at the interface between the ice shelves and the ocean (i.e. basal melt). We thus neglect the meltwater produced underneath the ice sheet in the subglacial hydrologic system [*De'Ath et al.*, 2014] because of the large uncertainties surrounding the magnitude of this source [*Hawkings et al.*, 2014] but we acknowledge that it may be an important component of meltwater Fe delivery. We also neglect the contribution of particulate iron whose concentrations are known to be very high in front of the ice shelves [*Sherrell et al.*, 2015; *Gerringa et al.*, 2012]. Further studies will be required to properly represent the potentially-important interactions between the particulate iron and the dFe inventory.

The physical model provides the location, time and magnitude of glacial meltwater production at the base of the ice shelves. This information determines the rate at which the Eulerian tracer is released in the model. The tracer concentration is converted into a dFe concentration by multiplying by an end-member for 'pure' glacial meltwater. *McGillicuddy et al.* [2015] assumed an end-member of 29 ± 21 nM based on Antarctic glacial ice cores while *Gerringa et al.* [2012] mentions values of 20–50 nM. For the purpose of this study, we estimate the gmw end-member ($\phi_{\text{gmw}}^{\text{dFe}}$) from the water column data collected in front of the Dotson ice shelf [*Sherrell et al.*, 2015]:

$$\text{dFe} = (1 - c_{\text{gmw}})\, \phi_{\text{background}}^{\text{dFe}} + c_{\text{gmw}}\, \phi_{\text{gmw}}^{\text{dFe}}, \tag{2}$$

where 'dFe' is the dissolved iron concentration measured in the outflow of the Dotson (0.7 nM), c_{gmw} the observed glacial meltwater fraction [15 ppt, assumed to be entirely of sub-ice shelf origin; *Randall-Goodwin et al.*, 2015], and $\phi_{\mathrm{background}}^{\mathrm{dFe}}$ is a 'background' dFe concentration from all other iron sources. Using as an initial estimate $\phi_{\mathrm{background}}^{\mathrm{dFe}} \sim 0.37$ nM for the background (i.e. the dFe concentration in CDW at the shelf break) leads to a meltwater end-member concentration of 22 nM. For the present study we round to a conservative value of $\phi_{\mathrm{gmw}}^{\mathrm{dFe}} = 20$ nM.

The initial condition for the glacial meltwater tracer is $c = 0$ ppt (i.e. no tracer inside the model domain on Jan. 1, 2006). A combination of radiation and nudging to zero is applied to the tracer inside 50 km-wide buffer zones positioned at the open boundaries [*Marchesiello et al.*, 2001]. With this choice of open boundary, we effectively neglect the contributions from outside sources (e.g. from the Bellingshausen Sea). The tracer accumulates over time in the model domain until a balance is reached between the tracer injection and the outward transport at the open boundaries. This outward transport corresponds to a westward coastal current directed toward the Ross Sea [e.g., *Nakayama et al.*, 2014]. A period of 10–12 years is typically required for the tracers to reach a stationary state in this model domain.

2.3.3 Deep sediments

The high dFe concentrations observed near the sea floor represent an important component of the dFe distribution and may play a substantial role in the iron supply of the ASP. However, the limited data and the uncertainties surrounding the nature of the bottom intensification make its incorporation in the model difficult. Our approach is to simply prescribe a fixed dFe concentration in the deepest vertical level of the model at every point on the continental shelf [a Dirichlet boundary condition; e.g., *Mack et al.*, 2017]. The dFe concentration of the deepest model level is informed by the observations while the concentrations above the deepest model level are calculated from the modeled advection and diffusion. This approach may overestimate the contribution of the sediments since a constant dFe in the deepest model level represents an infinite reservoir of dFe. On the other hand, if there is a benthic dFe source from the shallower regions that is swept away quickly by the ocean circulation (so it does not appear as a near-bottom enrichment in the observations), then the approach is underestimating the dFe input from sediments in these regions. An alternative approach would be to prescribe a dFe flux at the bottom (Neumann boundary condition) but no observational estimates of such a flux are available for this system, and the uncertainties in assigning or parameterizing such fluxes are very large [*Aumont et al.*, 2015; *Tagliabue et al.*, 2016].

The profiles of *Sherrell et al.* [2015] provide information on the bottom dFe concentrations throughout the ASP (Figure 6a). The contribution from sediments is defined by concentrations below 300 meters that are in excess of 0.35 nM. This 'background' concentration of 0.35 nM is assumed to originate from all sources other than sediments, and areas shallower than 300 m are assumed to have no sediment input. Comparison between observed bottom concentrations and the local depth indicates that bottom dFe increases with bottom depth (Figure 6c). The result from a linear regression of local depth and bottom concentrations is compared to the observed values in Figure 6d. The linear regression qualitatively captures the spatial variations but a large overestimation (underestimation) is apparent at Station 5 (Station 48). These variations are to be expected considering the uncertainties surrounding

this source of dFe (see Section 1). The simple linear relationship should be viewed as a first attempt toward representing the dFe from sediments.

The linear regression must be slightly modified to account for the fact that the model concentrations are defined at mid-height within the model levels. In other words, the bottom concentration from the data must be extrapolated between 20 m (Bear Ridge, Fig. 1) and 60 m (deepest glacial troughs) above the sea floor. Following *Mack et al.* [2017] and *Marsay et al.* [2014], we assume that dFe concentrations decrease exponentially away from the bottom (Figure 6b). A regression to an exponential function suggests an *e*-folding length scale of 205 m, which is used to extrapolate the bottom values above the sea floor. A concentration of zero is assumed outside of the continental shelf, at the model open boundaries, and within the ice shelf cavities. The latter implies that all the sediment tracer present within the ice shelf cavities must have been transported in by the ocean circulation. It also implies that the model may be underestimating the contribution from sediments.

The initial condition of the tracer is zero everywhere on Jan. 1, 2006. The tracer is then gradually introduced in the deepest model level with a nudging timescale of 10 days. This nudging takes place throughout the simulation to maintain the concentration of the deepest model level. The nudging is deactivated when the local concentration exceeds the prescribed value (i.e. greater than the value for the relevant bottom depth, as derived from the linear regression).

2.3.4 Sea ice

Antarctic sea ice is associated with dFe concentrations that vary substantially depending on season and location. Measured concentrations vary between 1.1 and 30.2 nM in west Antarctica alone with median values ~ 5 nM (*Lannuzel et al.* [2010]; see *Lannuzel et al.* [2016] for a review). For the purpose of this study, we assume that sea ice has a uniform concentration of 5 nM and that the dFe released is proportional to the simulated production of sea ice meltwater. This calculation provides the location and magnitude of the dFe flux associated with sea ice melt. For simplicity, we do not explictly represent the dFe from snow on top of the sea ice and assume it is included within the 5 nM end-member. Our focus on the supply of dFe also leads us to neglect any removal of iron from the ocean surface during the growth of sea ice [e.g., *Lannuzel et al.*, 2016]. Sea ice thus only acts as a source of dFe during the summer period.

2.4 Perturbation experiments

2.4.1 Preventing the deep tracers from exiting the ice shelf cavities

The idealized experiment includes two 'deep' sources of dFe: CDW and sediments. The dFe associated with these deep sources remains unavailable for primary production unless a physical mechanism is able to transport the dFe into the upper 100 m. For example, wintertime vertical mixing can reach down to depths of 400 m in the ASP [see the temperature profiles in Figure 2a of *Sherrell et al.*, 2015]. Other potential mechanisms would be iceberg melting or the ice shelf melt-driven circulation inside ice shelf cavities [*Greisman*, 1979]. The latter mechanism ('meltwater pump') is analogous to a traditional estuarine circulation with

ice shelf melt in place of the river discharge. In the case of the Amundsen Sea, the very high melt rates lead to a particularly vigorous circulation that extends beyond the cavities: *Jourdain et al.* [2017] estimate that the meltwater pump circulation drives 45% of the horizontal barotropic circulation in the eastern Amundsen Sea. In the context of this study, the important component of the 'meltwater pump' is the vertical (upward) transport of properties such as deep nutrients inside the ice shelf cavities.

We conduct a perturbation experiment to examine the relative importance of the latter mechanism in the vertical distribution of the deep dFe sources (CDW and sediments). Two additional Eulerian tracers representing dFe from CDW and sediments are implemented in the model. The two tracers are identical to the original ones (Sections 2.3.1, 2.3.3) except that their concentration is relaxed to zero inside the ice shelf cavities (relaxation timescale of 10 days). This relaxation effectively prevents the two tracers from exiting the ice shelf cavities (the cavities acting as a 'black hole'). With this modification, vertical mixing on the continental shelf becomes the only mechanism available for the upward transport of the deep dFe tracers. Comparison between the original tracers and the modified tracers allows us to determine the relative importance of the physical mechanisms. Note that the physics (currents, vertical diffusivity) remain identical in the control and perturbation experiments; only the two tracers are affected. A complete shutdown of the meltwater pump circulation (e.g. by setting basal melt rates to zero) is not attempted as this would substantially affect the coastal circulation [*Jourdain et al.*, 2017].

2.4.2 Idealized biological drawdown and replenishment of the upper 100 m

The stationary tracer distribution does not provide information on the seasonality of the dFe inventory as it neglects the biological drawdown taking place during summer (among other related processes). This seasonal cycle of the dFe inventory is conceptualized in Figure 7. We hypothesize that iron concentrations in the upper layers are relatively abundant and stable during the period preceding the sea ice breakup, with values around 0.3 nM [i.e. the concentration of Winter Water, *Sherrell et al.*, 2015]. We will refer to this 'pre-bloom' inventory as the winter reserve [e.g., *McGillicuddy et al.*, 2015]. Then, the biological drawdown would gradually decrease the inventory of the upper layers from early December to mid-March (corresponding to the closing of the polynya). Finally, vertical mixing and other physical processes would replenish the upper layers.

The replenishment process is likely to be dominated by physical processes (rather than biogeochemical processes since the period of biological production will be over) and thus can be simulated with the passive tracers. Such an experiment provides valuable information on the rate at which each dFe source replenishes the upper 100 m of the ASP after the biological drawdown of the summer season. One biogeochemical process that could still be significant during this period would be recycling, but its effect would be mostly to accelerate the replenishment. The experiment follows these steps: (1) We define a control volume representing the polynya during the month of January [i.e. the peak production period, see *Arrigo et al.*, 2015]. This control volume (described in more detail below) is constant in time. (2) The passive tracers are initialized at the beginning of the model simulation (Jan. 1, 2006) to the stationary distribution obtained after 13 years of spinup. (3) On March 15 of every year (closing of polynya and end of production period), the tracer concentrations are multiplied by

a non-dimensional profile of the form:

$$
\xi(z) \quad \equiv \quad
\begin{cases}
0 & \text{if } z \geq -100\,\text{m}, \\
-50^{-1}\,(z + 100\,\text{m}) & \text{if } -150\,\text{m} < z < -100\,\text{m}, \\
1 & \text{if } z \leq -150\,\text{m},
\end{cases}
\tag{3}
$$

where $z < 0$ is the depth (0 at surface). The multiplication by $\xi(z)$ artificially removes the tracers in the upper layers of the model and mimics a seasonal drawdown. For comparison, the median dFe concentrations in profiles observed during ASPIRE (representative of conditions in early/peak bloom) show values of $\sim 0.3\,\text{nM}$ at $150\,\text{m}$ decreasing linearly to $\sim 0.1\,\text{nM}$ at $25\,\text{m}$. The idealized drawdown of Eq. 3 is applied over the entire model domain for simplicity (the horizontal extent of the iron-depleted surface layers in March is unknown, and possibly much larger than the polynya owing to the ocean circulation during the production period). Although this simplification can underestimate the rate of replenishment by limiting lateral inputs, the model suggests that it is vertical mixing that plays a primary role in this process (Section 3.6). (4) After March 15 of each year, the tracers gradually populate the control volume (replenishment) until their concentration reaches a stationary value again (Figure 7b). This idealized seasonal cycle is used to extract two important diagnostics: the rate at which each dFe source replenishes the control volume (Table 1), and the relative contribution of each dFe source to the 'winter reserve'. These diagnostics are calculated for each simulated year to provide an estimate of the interannual variability.

The control volume is assumed to have constant shape to simplify the analysis and interpretation of the results (see Figure 1 for its extent). The horizontal extent ($2.58 \times 10^{10}\,\text{m}^2$) represents the polynya in January and is calculated with a maximum 15% sea ice concentration threshold over a 6–year average of satellite-derived concentrations [AMSR-E, years 2006–2011, *Cavalieri et al.*, 2014]. The control volume extends vertically over the upper $100\,\text{m}$ to match the idealized drawdown (Eq. 3). For comparison, the average mixed layer depth from all profiles collected during ASPIRE is $49\,\text{m}$ with, presumably, deeper values in March (when the idealized drawdown is applied). Although the perturbation experiment includes several assumptions and idealizations, its goal is only to highlight the relative contribution of the tracers to the winter reserve and to estimate how quickly dFe is restored in the upper $100\,\text{m}$ of the polynya during the following winter. Using more sophisticated assumptions is unlikely to change the relative contribution of the dFe sources in this process.

Sea ice is different from the three other sources of dFe as it is not associated with a numerical tracer (see Section 2.3.4). Its contribution to the 'winter reserve' (Table 1) is thus defined in a different way. It is calculated as the annual sea ice melt over the polynya distributed over the control volume. No value is provided for the 'supply rate' of sea ice.

3 Results

3.1 Pathways of dissolved iron from glacial meltwater, CDW and sediments

The pathways of the numerical tracers representing subsurface sources of dissolved iron are largely determined by the mean ocean circulation on the continental shelf (which we describe briefly here). Connections between the continental slope and the continental shelf primarily occur on the northern end of three glacial troughs: the Dotson, Central and Eastern

troughs (Figure 8d). The Dotson trough is characterized by a clockwise circulation ('gyre') with its western, northward-flowing branch carrying water modified by glacial melt [*Ha et al.*, 2014]. The presence of a shallow ridge between the Dotson and Eastern troughs (Bear Ridge) limits their exchanges to a coastal current that flows westward along the front of the Thwaites, Crosson, Dotson and Getz ice shelves. In general, the mean circulation is qualitatively similar at different depths owing to the weak ambient stratification of Antarctic continental shelves.

The pathways of glacial meltwater are represented in a video (Supporting Information) and summarized in a schematic (Figure 8a). Glacial meltwater is mainly produced by four ice shelves: Pine Island Glacier (PIG, $\sim 100\,\mathrm{Gt\ year^{-1}}$), Thwaites ($\sim 100\,\mathrm{Gt\ year^{-1}}$), Dotson (DIS, $\sim 50\,\mathrm{Gt\ year^{-1}}$) and Getz ($\sim 150\,\mathrm{Gt\ year^{-1}}$) [*Rignot et al.*, 2013]. The model suggests that the outflow from PIG and Thwaites join together south of Bear Ridge before entering the ASP on its southeastern corner. Glacial meltwater follows two paths inside the polynya: a clockwise circulation around the edges of Dotson Trough, and a westward path along the front of the ice shelves. The latter path represents the main outlet for glacial meltwater [e.g., *Nakayama et al.*, 2014]. The video also highlights how the uneven topography forces a fraction of the glacial meltwater to be diverted northward and across the continental shelf. This is particularly apparent along the western edge of the Dotson Trough and in front of Siple/Carney Islands. Once it reaches the shelf break, the glacial meltwater gradually expands along the shelf break in the northeastward direction. The uneven topography is thus responsible for the large footprint of glacial meltwater on the continental shelf (e.g., Figure 4).

Circumpolar Deep Water intrudes over the continental shelf inside the Dotson, Central and Eastern troughs (Figure 8b and the video in Supporting Information representing CDW in the deepest model level). The deep water mass tends to flow southward along the bottom topography and eventually reaches inside the ice shelf cavities to form a clockwise circulation inside of them [e.g., *Jacobs et al.*, 2011]. It takes approximately six months for the CDW tracer to travel from the shelf break to the front of Pine Island Glacier (PIG). CDW typically exits the cavities along their western edge and at a shallower depth owing to the melt-driven overturning circulation (meltwater pump) inside the cavities [e.g., *Randall-Goodwin et al.*, 2015; *Jacobs et al.*, 2011]. This outflow becomes apparent after 1.5 years in the video representing CDW at 150 m depth (Supporting Information). The 'upwelled' CDW then continues its path westward along the ice shelf front in a manner similar to glacial meltwater.

The 'sediment' tracer is represented by a schematic (Figure 8c) and by two videos (deepest model level and 150 m depth; see Supporting Information). Because the parameterization demands that the sediment dFe source is greatest at deep bottom depths, the sediment tracer input is dominated by the trough regions and especially their deepest portions near the ice shelves (see Section 2.3.3). The parameterization assumes no sediment input from the regions shallower than 300 m (i.e. we neglect processes such as vertical mixing of sediments by icebergs over shoals). The tracer concentration is initially zero but concentrations in the deepest model level attain the value dictated by the parameterization after only a few weeks. At the same time, the tracer begins to circulate within the ice shelf cavities and re-emerges from their western edge at a shallower depth (see video representing the tracer at 150 m). The pathway of this 'upwelled' sediment tracer is similar to that of the upwelled CDW. It is primarily transported westward along the coast but also spreads in the northward direction at the locations mentioned earlier.

In summary, the three tracers exhibit similar features even though they represent very different dFe sources. The similarities arise from the fact that all three tracers participate in the vigorous melt-driven circulation underneath the ice shelves. Once they emerge from the cavities, the three tracers follow similar pathways dominated by the coastal current and by the cross-shelf topography.

3.2 Spatial distribution of dissolved iron from the tracers

The passive tracers representing dFe from glacial meltwater, CDW and deep sediments were integrated in time from zero on Jan. 1, 2006 for a period of 13 years (a 'spin-up'). This period of time corresponds to a full cycle of the model forcing (Jan. 2006 to Dec. 31, 2013, 8 years) followed by an additional five years (Jan. 1, 2006 to Dec. 31, 2010). The model physics (currents, vertical diffusion) are the same in the two integrations. The tracers require 10–12 years for their concentrations to stabilize but using 13 years allows us to match the time period of ASPIRE (Dec. 2010 to Jan. 2011). The model fields are averaged over the month of Dec. 2010 to minimize the signature of individual eddies.

We begin by examining the vertical distribution of the tracers along a north–south section for which observations are available (see Figure 1 for its location). The section goes from the Dotson ice shelf front to the shelf break. This comparison is only for the subsurface inventories and the role of sea ice-derived dFe will be examined separately (Section 3.4). Dissolved iron from glacial meltwater is ~ 0.15 nM in the upper 350 m and gradually decreases to near-zero values at 800 meters (Figure 9a). The main feature of the section is a rapid increase in dFe concentrations in the vicinity of Dotson ice shelf with a maximum concentration of 0.3 nM. North of this input, dFe drops off fairly quickly but remains maximal in the upper water column, until reaching rather uniform distribution in the outer third of the continental shelf. The model suggests that the gmw-derived dFe extends 10–30 km past the shelf break (Figure 4) and thus could provide dFe to the regions offshelf.

The dFe from the CDW tracer has a relatively uniform vertical distribution (Figure 9b). Concentrations are 0.15–0.2 nM over most of the water column with a slight increase toward the bottom (0.25 nM). Higher concentrations (0.3 nM) are apparent near the shelf break because of the proximity to the tracer source at the shelf break (see Section 2.3.1). A slight increase in dFe concentration is apparent near Dotson ice shelf (0.2 nM up to 300 m), indicating that this deep dFe source is mobilized by the ice shelf melt circulation.

The dFe from sediments is dominated by a ~ 300 m thick iron-rich bottom layer inside the Dotson trough (40 km to 275 km in Figure 9c). dFe concentrations decrease from 0.7 nM at 700 m to 0.3 nM at 450 m. The concentrations shallower than 400 m depth are more uniform with values ~ 0.2 nM. As for the other deep dFe source (CDW), a 0.1 nM increase in concentration is apparent in front of the Dotson ice shelf up to 100 m depth.

The dFe from these three subsurface sources is combined in Figure 9d for comparison with the observations (Figure 9e). Starting from the bottom (750 m to 500 m depth), the sediment tracer represents the most important contributor to the total dFe inventory and is essential to reproduce the large dFe values observed near the bottom (> 1 nM). However, the linear regression for the bottom concentration of this source (see Section 2.3.3) overestimates

the horizontal extent of the iron-rich sediments. For example, the observed dFe decreases abruptly southward of 50 km and northward of 160 km (Figure 9e). The vertical extent of the sediment-derived dFe appears to be reasonably captured by the model (0.5 nM versus 0.6 nM at 450 m depth).

At the front of the Dotson ice shelf, the modeled distribution qualitatively captures the high dFe concentrations corresponding to the outflow from the ice shelf (Figure 9d,e). The modeled concentration is approximately 0.1 nM above the observed value (0.8 nM versus 0.7 nM). The modeled outflow extends higher in the water column than the observations, a feature that can be attributed to the glacial meltwater tracer (Figure 9a). Away from the ice shelf, and at depths shallower than 450 m, the modeled dFe concentrations are 1.67 times higher than the observations (~ 0.5 nM versus ~ 0.3 nM). These differences will be examined in more detail in the next figures.

The horizontal distribution of the simulated dFe inventory is presented for three different depth horizons: 500 m, 300 m and 150 m (Figures 10,11,12). The shallowest depth (150 m) is assumed to be sufficiently deep to minimize the signature of biological uptake (which is present in observations but absent from the model). At 500 m depth, glacial meltwater makes a small contribution to the dFe inventory (< 0.1 nM) while CDW and sediments provide comparable amounts of iron (~ 0.2 nM and ~ 0.4 nM on average over the shelf, respectively; Figure 10a,b,c). Both CDW and sediment tracers show relatively homogeneous concentrations over the continental shelf. Inside the ice shelf cavities, these two tracers tend to occupy the deepest areas of the cavity (see Supporting Information). The total inventory (Figure 10d) shows dFe concentrations between 0.6 nM and 0.8 nM with maximum values inside the ice shelf cavities. The simulated distribution is consistent overall with the observations but underestimates the spatial variability. Observed concentrations vary between 0.4 nM to 0.95 nM with no obvious pattern. These discrepancies between modeled and observed distributions can be linked to the linear regression for the sediment source (Figures 6c,d) and the lack of biogeochemical processes that contribute to the large variations from one station to another.

The modeled dFe concentration at shallower depths (300 m and 150 m) shows a decreasing contribution from the deep dFe sources (CDW and sediments) and an increased contribution from glacial meltwater (Figures 11, 12). The horizontal distributions are again fairly homogeneous owing to the topography-constrained cross-shelf excursions of the tracers (see Section 3.1). Nevertheless, the total dFe inventory reveals regional differences in dFe concentrations (Figures 11d, 12d). The westward coastal current generates a regional gradient, with lower dFe concentrations within the Eastern Trough (i.e. upstream of the ice shelves) and largest dFe concentrations in the southwestern regions (downstream of the ice shelves).

Comparison with observations at 300 m and 150 m again shows systematically higher values for the model (0.5 nM versus 0.3 nM) except within the outflow of the Dotson ice shelf where observed and modeled values are similar (Figures 11d,12d). The three subsurface dFe sources (glacial meltwater, CDW and sediments) exhibit non-zero concentrations at these depths and all three contribute to the total modeled dFe inventory. A relatively large overestimation (~ 0.6 nM for the model, ~ 0.15 nM for data) is apparent at a depth of 150 m in front of the Getz ice shelf (Station 5; see Figure 6d for the location of the stations). A closer examination of the dFe data at this station reveals low concentrations < 0.2 nM extending

from the surface down to unusually large depths [250 m; see *Sherrell et al.*, 2015, their Figure 3d]. A potential cause for this model-data discrepancy would be wind-driven downwelling of dFe-depleted surface water at the front of the Getz ice shelf (mean winds are generally westward while the ice shelf front is oriented west-east, representing conditions consistent with downwelling; *Kim et al.* [2016a]).

3.3 Oceanic circulation in the vicinity of ice shelves

The previous sections illustrated the important role played by the ice shelf melt-driven circulation (the 'meltwater pump') in the dFe distribution simulated by the model. In this section we examine in more detail the effect of the meltwater pump on the tracers' pathways. We specifically focus on the Dotson ice shelf because of its proximity to the ASP, which was extensively sampled during ASPIRE.

The ocean circulation in front of the Dotson was measured with an on-board Acoustic Doppler Current Profiler (ADCP) at an approximate distance of 200 m from the ice shelf [Figure 13a, *Randall-Goodwin et al.*, 2015]. The data reveal a strong outflow (velocity up to 30 cm s^{-1}) along the western edge of the ice shelf cavity. The outflow is concentrated between 100–400 m depth. The outflow is compensated by a broader, deeper inflow along the eastern edge of the cavity. The inflow is apparent below 400 m depth and shows velocities of 10–20 cm s^{-1}. The overall pattern suggests a clockwise circulation within the ice shelf cavity. The height difference between the inflow and outflow also suggests an upward flow inside the cavity.

To compare with these observations, the model fields were averaged over the month of Dec. 2010 and sampled along the grid points forming the ice shelf front. Such an 'ice shelf front' is not clearly defined in the model since the transition between ice shelf draft [$\sim$ 250 m, *Schaffer et al.*, 2016] and open ocean (0 m) takes place over a few grid points. For the purpose of this comparison, the model fields were thus sampled halfway through the transition zone, defined by an ice shelf draft of $\sim$ 100 meters (other values lead to similar results). Horizontal ocean velocities were projected along the ice shelf draft gradient (approximately north/south) to represent the inflow/outflow to the cavity. The model fields cover the entire width of the ice shelf and thus extend slightly farther than the observations (113.5°W versus 113.3°W on the western side, and 112.1°W versus 112.0°W on the eastern side; see Figure 13a,b).

The simulated flow at the model ice shelf front shows features that are consistent with the ADCP section (Figure 13a,b). A strong outflow of 25 cm s^{-1} is apparent along the western edge of the cavity. The outflow is relatively narrow ($\sim$ 7 km) and confined between 100 m and 400 m. A broader ($\sim$ 20 km) and slower inflow is present on the eastern side and concentrated below 400 m depth. The outflow coincides with enhanced glacial meltwater concentrations (Figure 13b,c) as expected. A considerably weaker outflow is also apparent below 600 m (easting $\sim$ 25 km) and reduces the overall inflow to the cavity.

The effect of the meltwater pump on the distribution of the deep dFe sources (CDW and sediments) is particularly apparent along the ice shelf front (Figure 13d,e). Sediment-derived dFe concentrations within the outflow are $\sim$ 0.15 nM above the rest of the section (0.4 nM versus 0.25 nM). It implies that the meltwater pump effectively mobilizes the deep dFe and

transports it into the upper 300 m of the water column. The same feature is apparent for the other deep dFe source (CDW) but to a lesser extent (Figure 13d). The dFe concentrations inside the outflow are ~ 0.3 nM for glacial meltwater, 0.2 nM for CDW, and 0.375 nM for sediments. The total (0.875 nM) is comparable to the observed outflow (0.7 nM; Figure 9e).

3.4 Dissolved iron from sea ice melt

In this section we examine the contribution of sea ice to the dFe inventory of the ASP. This contribution is estimated from an end-member concentration of 5 nM and by using sea ice melt as a proxy for the release of ice-borne iron (Section 2.3.4). The two polynyas of the Amundsen Sea (ASP and Pine Island Polynya) are associated with south-easterly winds that act to drive sea ice away from the coasts [e.g., *Nihashi and Ohshima*, 2015]. The near-open water conditions favor oceanic heat loss and a continuous cycle of ice growth and ice export to the surrounding areas (a 'latent-heat' polynya). The simulated ice–ocean melt flux over the ASP is thus strongly asymmetrical and dominated by sea ice growth (Figure 14b). The bulk of the growth takes place from March to June with maximum production in April. Sea ice melt is limited to December–February and reaches its maximum in January (Figure 14b), which is approximately one month after the south-easterly winds initiate the opening of the polynya [mid-December, *Stammerjohn et al.*, 2015]. The total amount of sea ice melt over the ASP in January depends on the timing of the opening (an earlier date meaning less melt over the ASP). The total melt over the ASP in January is thus highly variable from one year to another ($\pm 40\%$, Figure 14b).

The spatial distribution of sea ice melt in January (month of maximum melt) is characterized by relatively little melt in the central part of the ASP and in front of PIG (0.1–0.2 m, Figure 14a). In the ASP the melt is concentrated along the outer edge of the polynya as expected from the dominant south-easterly winds. The modeled distribution is qualitatively consistent with the data analysis of *Randall-Goodwin et al.* [2015] where sea ice meltwater fractions are generally negative inside the polynya (indicating net ice growth) and slightly positive along its edges (net ice melt).

The role of the ASP as a net sea ice producer as well as the timing of the melt (~ 1 month after the polynya opens) tend to limit the contribution of sea ice to the dFe inventory. Assuming that the meltwater is distributed over a mixed layer depth $\Delta z = 49 \pm 30$ m in January, the polynya-averaged melt for this particular month ($h_{\text{melt}} \sim 0.30 \pm 0.12$ m, Figure 14b) translates to an increase in dFe concentration of 0.03 ± 0.03 nM:

$$\delta\text{dFe} = \frac{5\mu\text{moles}}{\text{m}^3} \times \frac{h_{\text{melt}}}{\Delta z} = 0.03 \pm 0.03\,\text{nM}. \tag{4}$$

Similarly, a meltwater thickness of 0.5 m (edges of ASP) or 0.15 m (eastern side of polynya) would create an increase (δdFe) of 0.05 ± 0.03 nM and 0.015 ± 0.010 nM, respectively. All these values are smaller or comparable to the lowest dFe concentrations measured during ASPIRE (~ 0.1 nM), and several times smaller than the other sources considered (e.g., Figure 9). These results are qualitatively consistent with the lack of surface dFe enrichment at ASPIRE stations [*Sherrell et al.*, 2015].

3.5 Perturbation experiment: Preventing the deep tracers from exiting the cavities

A perturbation experiment is conducted to evaluate the relative importance of vertical mixing on the continental shelf and the 'meltwater pump' in the vertical distribution of the tracers (see Section 2.4.1). In this experiment, the tracers are prevented from exiting the ice shelf cavities and thus vertical mixing is the only mechanism available for the upward transport of the deep dFe tracers (CDW and sediments).

In the case of the dFe from sediments, the control and perturbation experiment show similar concentrations near the sea floor (Figure 15a,b) as these are largely determined by the nudging in the deepest model level (see Section 2.3.3). The differences become greater while moving up in the water column. At 500 m depth, the dFe concentration is halved compared to the control simulation (0.2 nM versus 0.4 nM; Figure 15a,b). The concentration at 350 m is ≤ 0.1 nM compared to 0.3 nM for the control simulation. The large differences between the control and perturbation experiment indicate that the ice shelf melt-driven circulation is a major component of the circulation on the shelf [e.g., *Jourdain et al.*, 2017] and that it is largely responsible for the vertical distribution of the dFe from deep sediments.

The differences between the control and perturbation experiment are even greater in the case of the CDW tracer (Figure 15c,d). Preventing the CDW from circulating through the ice shelf cavities leads to deep distributions that are completely unrealistic, again highlighting that the melt-driven circulation is critical to the movement of all water masses on the continental shelf. The lack of CDW near the bottom inhibits vertical mixing and lead (along with the absence of 'meltwater pump') to unrealistically low concentrations in the upper 300 m ($<$ 0.1 nM). Overall, the two modified tracers confirm that the presence of 'deep dFe' in the upper 300 m of the water column is primarily the result of the meltwater pump circulation (Figure 13) rather than local vertical mixing.

3.6 Perturbation experiment: Idealized drawdown during the summer

A perturbation experiment with an idealized seasonal drawdown is conducted to simulate the post-bloom 'replenishment' of the iron inventory of the upper 100 m (see Section 2.4.2). The experiment provides two valuable diagnostics: the rate at which each dFe source supplies the upper 100 m of the ASP, and the contribution of each dFe source to the pre-bloom inventory (winter reserve). The diagnostics are calculated every model year to estimate the interannual variability.

The dFe inventory (average concentration in the upper 100 m) of the three Eulerian tracers follows a similar seasonality from one year to another (Figure 16). After the idealized drawdown (March 15), the inventories rapidly build up over a period of 3–4 months (March–June) and then continue increasing at a slower rate. The maximum dFe inventory is reached around October–January, after which the tracer concentrations slowly decrease until the next drawdown.

These seasonal variations are dictated by the physical advection and diffusion which evolve over seasons. For example, the rapid build-up in the months following March corresponds to the period of maximum sea ice growth (Figure 14b) and brine rejection over the

ASP. This process effectively mixes the upper layers and drives the quick replenishment of the control volume (see Supporting Information). Lateral injections at the ice shelf front ('meltwater pump') also contribute to the replenishment, but this contribution is fairly steady over the year. Finally, the slow decrease in the inventory between January and March corresponds to a speed-up of the coastal current during the ice–free period (Supporting Information). The faster coastal current transports dFe away from the ice shelves and produces a noticeable decrease in the inventory of the control volume.

The time-series of Figure 16 are used to quantify the relative contribution of each dFe source; the results are summarized in Table 1. The idealized experiment suggests that glacial meltwater and sediments make a similar contribution (0.17 nM, or 34% each) to the 'winter reserve'. This reserve is defined as the dFe inventory in the upper 100 m of the control volume between Oct. 1 and Jan. 1 ($\sim$ 0.5 nM, Table 1; note that this value is higher than the dFe concentration of Winter Water (see Discussion)). The similar contributions of glacial meltwater and sediments derive from the fact that the two sources have comparable concentrations at the base of the control volume (Figures 9a,c, 12a,c) and are affected by the same physical advection/diffusion. The other dFe sources make smaller contributions and provide 26% (CDW) and 5% (sea ice) of the winter reserve, respectively.

The interannual variability of these contributions is generally small over the eight years of simulation (2006–2013). Sea ice is the dFe source that fluctuates the most ($\pm$40%; see Section 3.4) but it remains the smallest dFe source in importance (Table 1). The interannual variability in the contributions of glacial melt, sediment and CDW to the winter reserve is 0.01-0.02 nM (Table 1). This represents only 15% of their average contribution to the winter reserve. The contributions from the three subsurface dFe sources tend to co-vary over 2006–2013 (Figure 16) with the largest inputs occurring in 2009 and 2013. The similar variability is expected from the fact that all subsurface dFe sources are subject to the same idealized drawdown and the same physical advection/diffusion. Although the limited number of years precludes a quantitative analysis of the interannual variability, we note that the year 2013 corresponds to relatively low modeled basal melt rates but high sea ice production within the polynya, emphasizing again the role of vertical mixing in the replenishment of the upper 100 m.

The rates at which the dFe sources replenish the control volume vary between 0.023 nM month^{-1} (CDW) and 0.036 nM month^{-1} (glacial ice and sediment; Table 1). The ratio between these rates is consistent with the concentration of these dFe sources at the base of the control volume ($\sim$ 0.15 nM for CDW, $\sim$ 0.2 nM for glacial ice and sediment; Figures 9, 12) and their contribution to the winter reserve (0.13 nM for CDW, 0.17 nM for glacial ice and sediment; Table 1). In other words, the supply rates reflect the relative abundance of the dFe sources at the base of the control volume, consistent with a replenishment that would be driven by vertical mixing in March–June.

4 Discussion and Summary

Several studies have highlighted the importance of dissolved iron [*Alderkamp et al.*, 2015] and glacial meltwater [*Gerringa et al.*, 2012; *Arrigo et al.*, 2015] in the high productivity of the ASP. As a first step toward understanding the iron supply of the ASP and its relation to

primary production, we implemented four plausible sources of dFe into a realistic model of the Amundsen Sea. The model is integrated in time to derive steady dFe distributions for each of these sources and the distributions are directly compared with *in situ* observations from the summer period.

The simulated dFe distributions exhibit three important features: an east-west gradient in dFe concentrations generated by the westward oceanic circulation, the dispersion of the dFe sources across the continental shelf caused by the uneven shelf topography [e.g., along the western edge of the Dotson Trough, *Ha et al.*, 2014], and the necessity of including the dFe from sediments to reproduce the observed bottom intensification. Although this picture obtained with conservative tracers is necessarily incomplete, the total dFe concentrations provided by the four sources are comparable to observed profiles. In the depth range 150-300 m, these modeled dFe concentrations are within a factor of 1.67 of the observations (0.5 nM versus 0.3 nM).

The main reason for this overestimation is likely to be the lack of iron scavenging and biological uptake. Both processes act to remove iron from the upper 150 m [*Bruland et al.*, 2014] and are currently absent from the model. Scavenging is particularly vigorous during the production period when organic particles are abundant throughout the upper layers and present many opportunities for adsorption. Nonbiogenic particles, notably in the vicinity of the ice shelves, can also be important as dFe scavengers. The overestimation of the simulated dFe concentrations emphasizes that such biogeochemical processes play a critical role in dissolved iron dynamics.

The surface-biased structure of simulated glacial meltwater (Figure 3) may play a secondary role in the overestimation of the dFe concentrations. Such a bias is to be expected from the lack of tidal mixing within the ice shelf cavities of the model [e.g., *Jourdain et al.*, 2017; *Robertson*, 2013]. Unresolved small-scale physical processes within the outflow of ice shelves [*Garabato et al.*, 2017] may also contribute to this model bias. Finally, the high bias in the melt of Getz and the large uncertainties in the bathymetry north of Getz ice shelf [*Kalén et al.*, 2016; *Nitsche et al.*, 2007] can both influence the glacial meltwater distributions.

The model results support the view that the fast-melting ice shelves in the Amundsen Sea make a critical contribution to the iron supply in the ASP [e.g., *Gerringa et al.*, 2012] in both a direct and an indirect manner. Direct injection of glacial meltwater is a key contributor to the dFe inventory of the upper 100 m in the experiment with idealized drawdown (34% of the winter reserve; Table 1). However, the results suggest that the fast-melting ice shelves also contribute indirectly to the iron supply through the 'meltwater pump' circulation (Figure 13). The latter is found to be primarily responsible for transporting dFe from sediments into the upper 300 m of the water column (Section 3.5) making this dFe source just as important as glacial meltwater (Table 1). More generally, the 'meltwater pump' circulation complements wintertime vertical mixing on the continental shelf [visibly limited to the upper 350 m; see the sections in *Jacobs et al.*, 2012] by providing a three-dimensional pathway for deep nutrients to be injected into the upper 300 m. The perturbation experiments suggest that, without this mechanism, the deep dFe sources would be largely inaccessible.

This role played by ice shelves is consistent with the correlation between chlorophyll concentrations and glacial melt reported by *Arrigo et al.* [2015]. The large differences in glacial

melt rates around the continent would imply that polynyas rely on different mechanisms for the bulk of their iron supply. For example, the Ross Sea is associated with considerably lower glacial melt rates [*Rignot et al.*, 2013] but also deep vertical mixing in several locations during winter [e.g., *Gordon et al.*, 2000]. In this case, the main supply mechanism would be vertical mixing and sediment-derived dFe [*Mack et al.*, 2017; *McGillicuddy et al.*, 2015].

Additional research will be required to further constrain the dFe dynamics of the ASP. Among the four sources, the dFe from sediments is possibly the least understood, with large variations between neighboring stations. A possible mechanism driving these variations involves sedimented particulate organic matter under the polynya bloom, helping to release iron from the sediments, either by supplying dissolved ligands during decay, or by consuming sufficient oxygen to drive shallow sediment reduction of Fe oxyhydroxides and release of soluble Fe(II) species to the water column. More generally, the coupling of the physical model with a biogeochemistry module will allow for a direct evaluation of the link between dFe supply and the primary production of the ASP.

References

Alderkamp, A. C., G. L. van Dijken, K. E. Lowry, T. L. Connelly, M. Lagerstrom, R. M. Sherrell, C. Haskins, E. Rogalsky, O. Schofield, S. Stammerjohn, P. L. Yager, and K. R. Arrigo (2015), Fe availability drives phytoplankton photosynthesis rates during spring bloom in the Amundsen Sea Polynya, Antarctica, *Elem. Sci. Anthropocene*, *3*(43), doi:https://doi.org/10.12952/journal.elementa.000043.

Arrigo, K. R., G. L. van Dijken, and A. L. Strong (2015), Environmental controls of marine productivity hot spots around Antarctica, *J. Geophys. Res. Oceans*, *120*, 5545–5565, doi:https://doi.org/10.1002/2015JC010888.

Aumont, O., C. Ethé, A. Tagliabue, L. Bopp, and M. Gehlen (2015), PISCES-v2: An ocean biogeochemical model for carbon and ecosystem studies, *Geosci. Model Dev.*, *8*, 465–2513, doi:https://doi.org/10.5194/gmd-8-2465-2015.

Biddle, L., K. Heywood, J. Kaiser, and A. Jenkins (2017), Glacial meltwater identification in the Amundsen Sea, *J. Phys. Oceanogr.*, *47*, 933–954, doi:https://doi.org/10.1175/JPO-D-16-0221.1.

Bruland, K. W., R. Middag, and M. C. Lohan (2014), Controls of trace metals in seawater, in *Treatise on Geochemistry*, edited by D. E. Carpenter and L. Dubbs, chap. 8.2, pp. 19–51, Elsevier, Hoboken, N.J., doi:https://doi.org/10.1016/B978-0-08-095975-7.00602-1.

Budgell, W. P. (2005), Numerical simulation of ice-ocean variability in the Barents Sea region: Towards dynamical downscaling, *Ocean Dyn.*, *55*, 370–387, doi:https://doi.org/10.1007/s10236-005-0008-3.

Cavalieri, D., T. Markus, and J. C. Comiso (2014), AMSR-E/Aqua daily L3 12.5 km brightness temperature, sea ice concentration and snow depth polar grids. Version 3 for 2006–2011, Boulder, Colorado USA: NASA DAAC at the National Snow and Ice Data Center, https://doi.org/10.5067/AMSR-E/AE_SI12.003.

Comiso, J. C. (1999), Bootstrap sea ice concentrations from Nimbus-7 SMMR and DMSP SSM/I-SSMIS, digital media, Nat. Snow Ice Data Center, Boulder, CO, USA.

De'Ath, R., J. L. Wadham, F. Monteiro, A. M. Le Brocq, M. Tranter, A. Ridgwell, S. Dutkiewicz, and R. Raiswell (2014), Antarctic ice sheet fertilises the Southern Ocean, *Biogeosciences*, *11*, 2635–2644, doi:https://doi.org/10.5194/bg-11-2635-2014.

Dee, D. P., S. M. Uppala, A. J. Simmons, P. Berrisford, P. Poli, S. Kobayashi, U. Andrae, M. A. Balmaseda, G. Balsamo, P. Bauer, P. Bechtold, A. C. M. Beljaars, L. van de Berg, J. Bidlot, N. Bormann, C. Delsol, R. Dragani, M. Fuentes, A. J. Geer, L. Haimberger, S. B. Healy, H. Hersbach, E. V. Holm, L. Isaksen, P. Kallberg, M. Kohler, M. Matricardi, A. P. McNally, B. M. Monge-Sanz, J.-J. Morcrette, B.-K. Park, C. Peubey, P. de Rosnay, C. Tavolato, J.-N. Thepaut, and F. Vitart (2011), The ERA-Interim reanalysis: Configuration and performance of the data assimilation system, *Quarterly Journal of the Royal Meteorological Society*, *137*, 553–597, doi:https://doi.org/10.1002/qj.828.

Dinniman, M. S., J. M. Klinck, and W. O. Smith Jr. (2011), A model study of Circumpolar Deep Water on the west Antarctic Peninsula and Ross Sea continental shelves, *Deep Sea Res. II*, *58*, 1508–1523, doi:https://doi.org/10.1016/j.dsr2.2010.11.013.

Fairall, C. W., E. F. Bradley, J. E. Hare, A. A. Grachev, and J. B. Edson (2003), Bulk parameterization of air-sea fluxes: Updates and verification for the COARE algorithm, *J. Clim.*, *16*, 571–591.

Garabato, A. N., A. Forryan, P. Dutrieux, L. Brannigan, L. C. Biddle, K. J. Heywood, A. Jenkins, Y. L. Firing, and S. Kimura (2017), Vigorous lateral export of the meltwater outflow from beneath an Antarctic ice shelf, *Nature*, *542*, 219–222, doi:https://doi.org/10.1038/nature20825.

Gerringa, L. J., A. C. Alderkamp, P. Laan, C. Thuroczy, H. J. De Baar, M. M. Mills, G. L. van Dijken, H. van Haren, and K. R. Arrigo (2012), Iron from melting glaciers fuels the phytoplankton blooms in Amundsen Sea (Southern Ocean): Iron biogeochemistry, *Deep-Sea Res. II*, *71-76*, 16–31, doi:https://doi.org/10.1016/j.dsr2.2012.03.007.

Gordon, L. I., L. A. Codispoti, J. C. Jennings, F. J. Millero, J. M. Morrison, and C. Sweeney (2000), Seasonal evolution of hydrographic properties in the Ross Sea, Antarctica, 1996-1997, *Deep Sea Res. II*, *47*(15-16), 3095–3117.

Greisman, P. (1979), On upwelling driven by the melt of ice shelves and tidewater glaciers, *Deep-Sea Res.*, *26A*, 1051–1065.

Ha, H. K., A. K. Wahlin, T. W. Kim, S. H. Lee, J. H. Lee, H. J. Lee, C. S. Hong, L. Arneborg, G. Bjork, and O. Kalen (2014), Circulation and modification of warm deep water on the central Amundsen Shelf, *J. Phys. Oceanogr.*, *44*, 1493–1501, doi:https://doi.org/10.1175/JPO-D-13-0240.1.

Hawkings, J. R., J. L. Wadham, M. Tranter, R. Raiswell, L. G. Benning, P. J. Statham, A. Tedstone, P. Nienow, K. Lee, and J. Telling (2014), Ice sheets as a significant source of highly reactive nanoparticulate iron to the oceans, *Nat. Commun.*, *5*(3929), doi:https://doi.org/10.1038/ncomms4929.

Hohmann, R., P. Schlosser, S. Jacobs, A. Ludin, and R. Weppernig (2002), Excess helium and neon in the southeast Pacific: Tracers for glacial meltwater, *J. Geophys. Res.*, *107*(C11), doi:https://doi.org/10.1029/2000JC000378.

Holland, D. M., and A. Jenkins (1999), Modeling thermodynamic ice–ocean interactions at the base of an ice shelf, *J. Phys. Oceanogr.*, *29*, 1787–1800.

Jacobs, S., A. Jenkins, H. Hellmer, C. Giulivi, F. Nitsche, B. Huber, and R. Guerrero (2012), The Amundsen Sea and the Antarctic Ice Sheet, *Oceanography*, *25*(3), 154–163, doi:https://doi.org/10.5670/oceanog.2012.90.

Jacobs, S. S., A. Jenkins, C. F. Giulivi, and P. Dutrieux (2011), Stronger ocean circulation and increased melting under Pine Island Glacier ice shelf, *Nat. Geosc.*, *4*, 519–523, doi:https://doi.org/10.1038/ngeo1188.

Jourdain, N. C., P. Mathiot, N. Merino, G. Durand, J. L. Sommer, P. Spence, P. Dutrieux, and G. Madec (2017), Ocean circulation and sea-ice thinning induced by melting ice shelves in the Amundsen Sea, *J. Geophys. Res. Oceans*, *122*, 2550–2573, doi:https://doi.org/10.1002/2016JC012509.

Kalén, O., K. M. Assmann, A. K. Wahlin, H. K. Ha, T. W. Kim, and S. H. Lee (2016), Is the oceanic heat flux on the central Amundsen sea shelf caused by barotropic or baroclinic currents?, *Deep-Sea Res. II*, *123*, 7–15, doi:https://doi.org/10.1016/j.dsr2.2015.07.014.

Kim, C., T. Kim, K. Cho, H. K. Ha, S. Lee, H. Kim, and J. Lee (2016a), Variability of the Antarctic coastal current in the Amundsen Sea, *Estuarine, Coastal and Shelf Science*, *181*, 123–133, doi:https://doi.org/10.1016/j.ecss.2016.08.004.

Kim, I., D. Hahm, T. S. Rhee, T. W. Kim, C. S. Kim, and S. Lee (2016b), The distribution of glacial meltwater in the Amundsen Sea, Antarctica, revealed by dissolved helium and neon, *J. Geophys. Res. Oceans*, *121*, 1654–1666, doi:https://doi.org/10.1002/2015JC011211.

Lannuzel, D., V. Schoemann, J. de Jong, B. Pasquer, P. van der Merwe, F. Masson, J. Tison, and A. Bowie (2010), Distribution of dissolved iron in Antarctic sea ice: Spatial, seasonal, and interannual variability, *J. Geophys. Res.*, *115*(G03022), doi:https://doi.org/10.1029/2009JG001031.

Lannuzel, D., M. Vancoppenolle, P. van der Merwe, J. de Jong, K. M. Meiners, M. Grotti, J. Nishioka, and V. Schoemann (2016), Iron in sea ice: Review and new insights, *Elem. Sci. Anthropocene*, *4*(130), doi:https://doi.org/10.12952/journal.elementa.000130.

Mack, S. L., M. S. Dinniman, D. J. McGillicuddy, P. N. Sedwick, and J. M. Klinck (2017), Dissolved iron transport pathways in the Ross Sea: Influence of tides and mesoscale eddies in a regional ocean model, *J. Mar. Syst.*, *166*, 73–86, doi:https://doi.org/10.1016/j.jmarsys.2016.10.008.

Marchesiello, P., J. C. McWilliams, and A. Shchepetkin (2001), Open boundary conditions for long-term integration of regional oceanic models, *Ocean Modell.*, *3*, 1–20.

Marsay, C. M., P. N. Sedwick, M. S. Dinniman, P. M. Barrett, S. L. Mack, and D. J. McGillicuddy (2014), Estimating the benthic efflux of dissolved iron on the Ross Sea continental shelf, *Geophys. Res. Lett.*, *41*, 7576–7583, doi:https://doi.org/10.1002/2014GL061684.

Mazloff, M. R., P. Heimbach, and C. Wunsch (2010), An eddy-permitting Southern Ocean state estimate, *J. Phys. Oceanogr.*, *40*(5), 880–899, doi:https://doi.org/10.1175/2009jpo4236.1.

McGillicuddy, D. J., P. N. Sedwick, M. S. Dinniman, K. R. Arrigo, T. S. Bibby, B. J. Greenan, E. E. Hofmann, J. M. Klinck, W. O. Smith, S. L. Mack, C. M. Marsay, B. M. Sohst, and G. L. van Dijken (2015), Iron supply and demand in an Antarctic shelf ecosystem, *Geophys. Res. Lett.*, *42*, 8088–8097, doi:https://doi.org/10.1002/2015GL065727.

Mellor, G. L., and L. Kantha (1989), An ice-ocean coupled model, *J. Geophys. Res.*, *94*, 10,937–10,954.

Millan, R., E. Rignot, V. Bernier, M. Morlighem, and P. Dutrieux (2017), Bathymetry of the Amundsen Sea Embayment sector of West Antarctica from Operation IceBridge gravity and other data, *Geophys. Res. Lett.*, *44*, 1360–1368, doi:https://doi.org/10.1002/2016GL072071.

Morales Maqueda, M. A., A. J. Willmott, and N. R. T. Biggs (2004), Polynya dynamics: A review of observations and modeling, *Rev. Geophys.*, *42*(RG1004), doi:https://doi.org/10.1029/2002RG000116.

Nakayama, Y., R. Timmermann, C. B. Rodehacke, M. Schroder, and H. H. Hellmer (2014), Modeling the spreading of glacial meltwater from the Amundsen and Bellingshausen Seas, *Geophys. Res. Lett.*, *41*(22), 7942–7949, doi:https://doi.org/10.1002/2014GL061600.

Nihashi, S., and K. I. Ohshima (2015), Circumpolar mapping of Antarctic coastal polynyas and landfast sea ice: Relationship and variability, *J. Clim.*, *28*, 3650–2670, doi:https://doi.org/10.1175/jcli-d-14-00369.1.

Nitsche, F. O., S. S. Jacobs, R. D. Larter, and K. Gohl (2007), Bathymetry of the Amundsen Sea continental shelf: Implications for geology, oceanography, and glaciology, *Geochemistry, Geophysics and Geosystems*, *8*(10), doi:https://doi.org/10.1029/2007GC001694.

Powers, J. G., K. W. Manning, D. H. Bromwich, J. J. Cassano, and A. M. Cayette (2012), A decade of Antarctic science support through AMPS, *Bulletin of the American Meteorological Society*, *November*, 1699–1712, doi:https://doi.org/10.1175/bams-d-11-00186.1.

Randall-Goodwin, E., M. P. Meredith, A. Jenkins, P. L. Yager, R. M. Sherrell, E. P. Abrahamsen, R. Guerrero, X. Yuan, R. A. Mortlock, K. Gavahan, A. C. Alderkamp, H. Ducklow, R. Robertson, and S. E. Stammerjohn (2015), Freshwater distributions and water mass structure in the Amundsen Sea Polynya region, Antarctica, *Elem. Sci. Anthropocene*, *3*(65), doi:https://doi.org/10.12952/journal.elementa.000065.

Rignot, E., S. Jacobs, J. Mouginot, and B. Scheuchl (2013), Ice-shelf melting around Antarctica, *Science*, *341*, 266–270, doi:https://doi.org/10.1126/science.1235798.

Robertson, R. (2013), Tidally induced increases in melting of Amundsen Sea ice shelves, *J. Geophys. Res. Oceans*, *118*, 3138–3145, doi:https://doi.org/10.1002/jgrc.20236.

Scambos, T., B. Raup, and J. Bohlander (2017), Images of Antarctic ice shelves, Boulder, Colorado USA: National Snow and Ice Data Center, http://dx.doi.org/10.7265/N5NC5Z4N.

Schaffer, J., R. Timmermann, J. Arndt, S. S. Kristensen, C. Mayer, M. Morlighem, and D. Steinhage (2016), A global, high-resolution data set of ice sheet topography, cavity geometry and ocean bathymetry, *Earth Syst. Sci. Data Discuss.*, *8*, 543–557, doi:https://doi.org/10.5194/essd-8-543-2016.

Shchepetkin, A. F., and J. C. McWilliams (2005), The Regional Oceanic Modeling System (ROMS): A split-explicit, free-surface, topography-following-coordinate oceanic model, *Ocean Model.*, *9*, 347–404, doi:https://doi.org/10.1016/j.ocemod.2004.08.002.

Sherrell, R. M., M. E. Lagerstrom, K. O. Forsch, S. E. Stammerjohn, and P. L. Yager (2015), Dynamics of dissolved iron and other bioactive trace metals (Mn, Ni, Cu, Zn) in the Amundsen Sea Polynya, Antarctica, *Elem. Sci. Anthropocene*, *3*(71), doi:https://doi.org/10.12952/journal.elementa.000071.

St-Laurent, P., J. M. Klinck, and M. S. Dinniman (2015), Impact of local winter cooling on the melt of Pine Island Glacier, Antarctica, *J. Geophys. Res. Oceans*, *120*, 6718–6732, doi:https://doi.org/10.1002/2015JC010709.

Stammerjohn, S. E., T. Maksym, R. A. Massom, K. E. Lowry, K. R. Arrigo, X. Yuan, M. Raphael, E. Randall-Goodwin, R. M. Sherrell, and P. L. Yager (2015), Seasonal sea ice changes in the Amundsen Sea, Antarctica, over the period of 1979–2014, *Elem. Sci. Anthropocene*, *3*(55), doi:https://doi.org/10.12952/journal.elementa.000055.

Tagliabue, A., O. Aumont, R. Death, J. P. Dunne, S. Dutkiewicz, E. Galbraith, K. Misumi, J. K. Moore, A. Ridgwell, E. Sherman, C. Stock, M. Vichi, C. Volker, and A. Yool (2016), How well do global ocean biogeochemistry models simulate dissolved iron distributions?, *Global Biogeochemical cycles*, *30*, 149–174, doi:https://doi.org/10.1002/2015GB005289.

Yager, P. L., R. M. Sherrell, S. E. Stammerjohn, A. C. Alderkamp, O. Schofield, E. P. Abrahamsen, K. R. Arrigo, S. Bertilsson, D. L. Garay, R. Guerrero, K. E. Lowry, P.-O. Moksnes, K. Ndungu, A. F. Post, E. Randall-Goodwin, L. Riemann, S. Severmann, S. Thatje, G. L. van Dijken, and S. Wilson (2012), ASPIRE: The Amundsen Sea polynya international research expedition, *Oceanography*, *25*(3), 40–53, doi:https://doi.org/10.5670/oceanog.2012.73.

Yager, P. L., R. M. Sherrell, S. E. Stammerjohn, H. W. Ducklow, O. M. Schofield, E. D. Ingall, S. E. Wilson, K. E. Lowry, C. M. Williams, L. Riemann, B. Bertilsson, A. C. Alderkamp, J. Dinasquet, R. Logares, A. J. Melara, L. Q. Mu, R. G. Newstead, A. F. Post, R. Swalethorp, and G. L. van Dijken (2016), A carbon budget for the Amundsen Sea Polynya, Antarctica: Estimating net community production and export in a highly productive polar ecosystem, *Elem. Sci. Anthropocene*, *4*(140), doi:https://doi.org/10.12952/
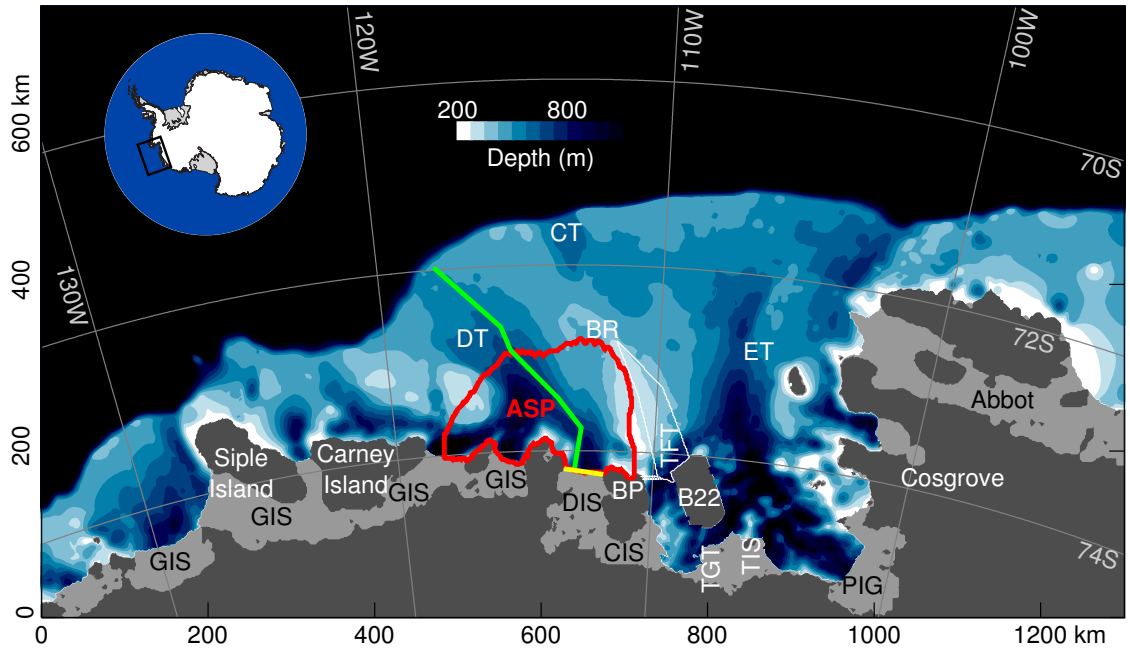
journal.elementa.000140.

Figure 1. Model domain with the main ice shelves labeled. The model open boundaries correspond to the edges of the figure. Color shading represents isobaths every 75 m. DT is Dotson Trough, CT is Central Trough, ET is Eastern Trough, BR is Bear Ridge, ASP is Amundsen Sea Polynya (red contour line), GIS is Getz Ice Shelf, DIS is Dotson Ice Shelf, BP is Bear Peninsula, CIS is Crosson Ice Shelf, TGT is Thwaites Glacier Tongue, TIS is Thwaites Ice Shelf, B22 is a large static iceberg, TFT is Thwaites Fast-ice Tongue, and PIG is Pine Island Glacier. The ASP represented is a climatological average for the month of January [years 2006–2011, *Cavalieri et al.*, 2014]. The green (yellow) line is the section of Figure 9 (13).
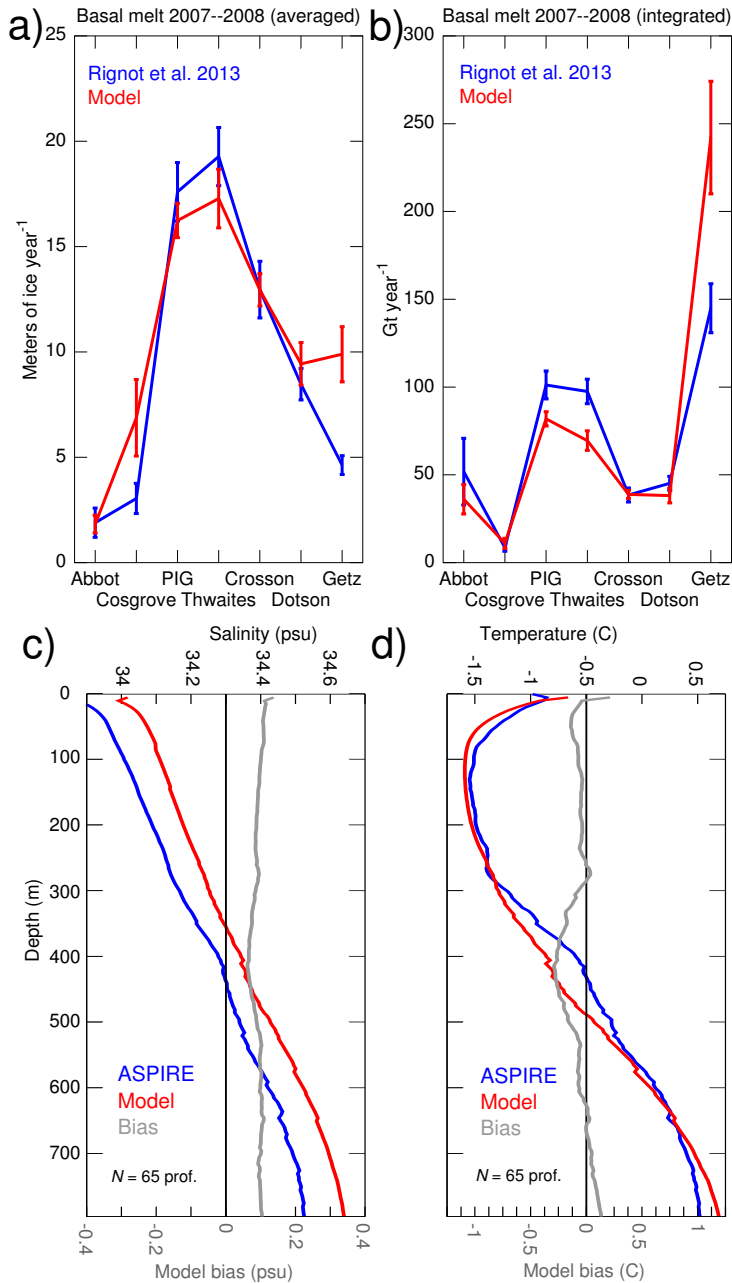
Figure 2. Model–Data comparison for basal melt rates, salinity and temperature. (a) Horizontally-averaged basal melt rate for years 2007–2008. Observed values [*Rignot et al.*, 2013] are converted to meters of ice assuming $920\,\mathrm{kg\,m^{-3}}$. Model error bars represent standard deviations over model years 2007–2008. (b) Same as (a) but horizontally-integrated over the area of the ice shelves. (c) Average salinity profile in the Amundsen Sea Polynya (ASP) from observations [blue, 65 profiles, *Yager et al.*, 2012] and from the model in Dec. 2010 (red). The model bias is in gray. (d) Same as (c) but for potential temperature.

–28–
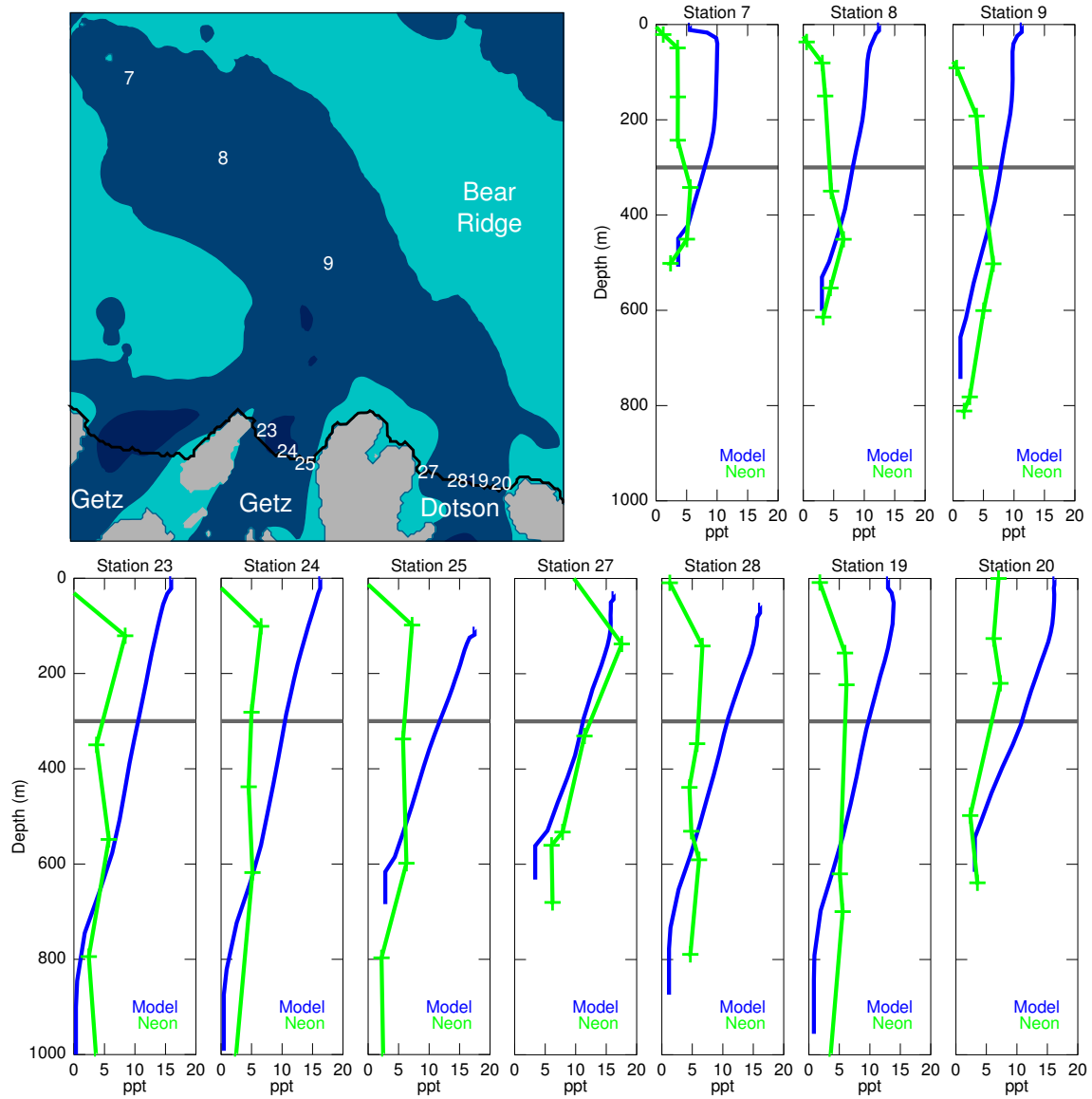
Figure 3. Model–data comparison for the vertical distribution of glacial meltwater. The data points are redrawn from *Kim et al.* [2016b] (data collected in January 2011 and February 2012). The horizontal dark gray line indicates the depth above which the data become uncertain [300 meters; see *Kim et al.*, 2016b]. The modeled glacial meltwater distribution is an average over the month of Dec. 2010 (13 years of spin-up). Note that modeled profiles extend from the model ice shelf draft to the model seafloor and may not match observed draft/depth.
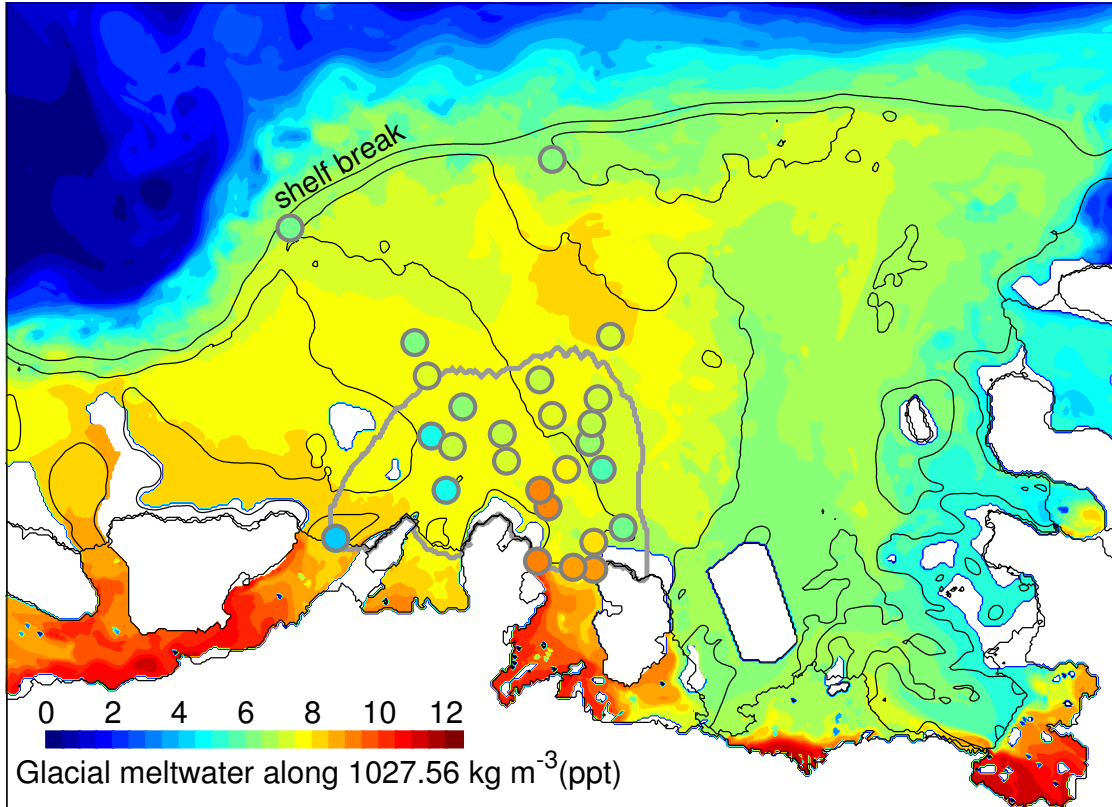
Figure 4. Model–data comparison for the horizontal distribution of glacial meltwater (gmw) along a deep density surface (1027.56 kg m^{-3}, approximately 450 m depth). Data points (circles) are from *Randall-Goodwin et al.* [2015] (data collected in December 2010—early January 2011). The simulated gmw represents an average over the month of Dec. 2010 (13 years of spin-up). The gray contour line is the control volume (climatological extent of the polynya in January). Black contour lines represent the ice shelf front, grounding line and 500 m/1000 m isobaths. Areas where the density surface intersects the sea floor or the surface appear in solid white.
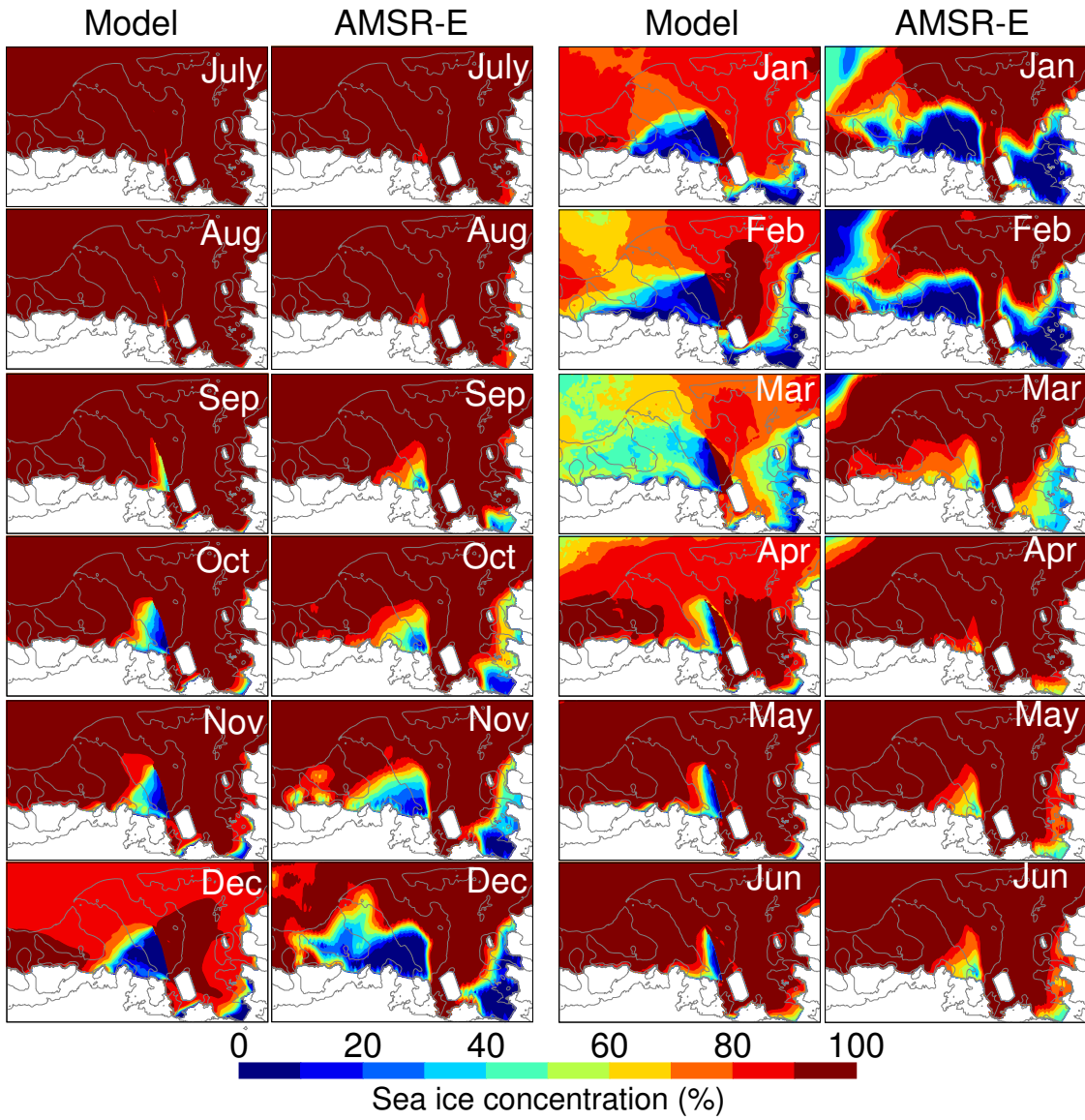
Figure 5. Model–data comparison for sea ice concentration (monthly averages, July 2010 to June 2011). The data are from *Cavalieri et al.* [2014]. The gray contour lines indicate the 500 m isobath, the grounding line and the ice shelf front. Grounded ice, ice shelves and icebergs are in solid white.
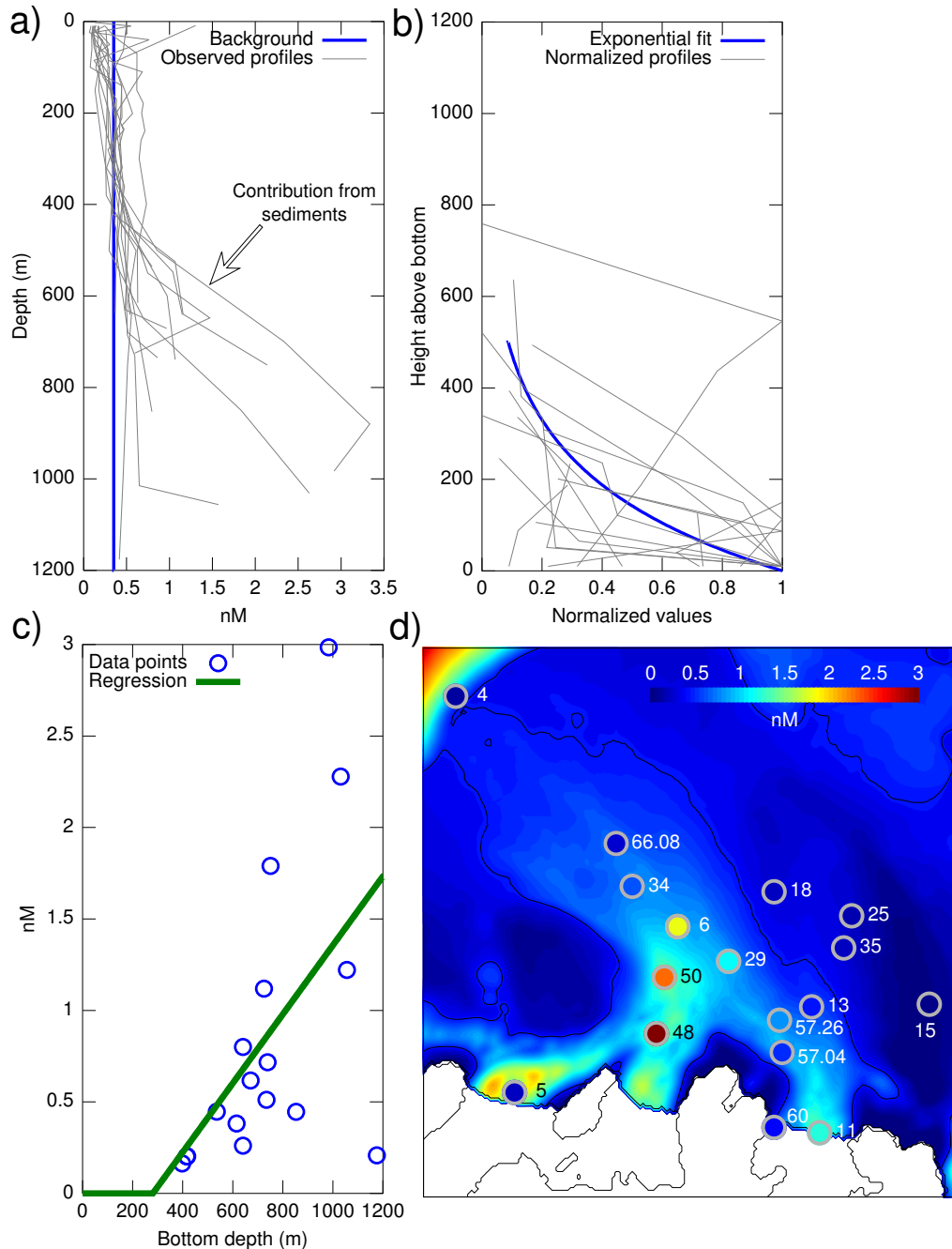
Figure 6. Parameterization of the tracer for sediments-derived dissolved iron (dFe). (a) Observed dFe profiles and contribution from sediments (defined as dFe>0.35 nM below 300 m depth). (b) Bottom portion (depth >400 m) of the observed dFe profiles. The profiles were normalized by substracting a background value (0.35 nM) and by dividing by the maximum concentration. The blue curve represents a regression to an exponential function. (c) Linear regression between dFe values at the bottom (excluding the background signal) and local depth. (d) Comparison between observed bottom dFe (circles with station number) and the linear regression (shading). The dFe concentrations exclude the background signal.
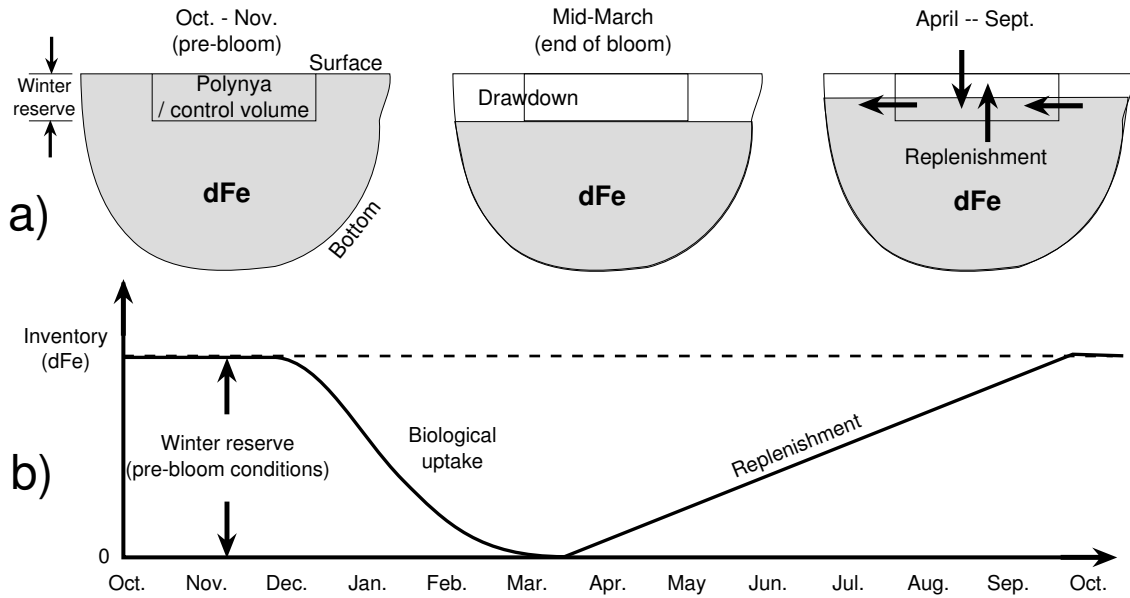
Figure 7. Conceptual model of the seasonal bloom in the Amundsen Polynya. (a) Schematic of the seasonal iron inventory (gray shading) in the Amundsen Sea. The rectangle represents the control volume (upper 100 m of the polynya in January). The 'replenishment' includes all vertical/lateral fluxes contributing to the formation of the pre-bloom inventory (winter reserve). (b) Seasonal iron inventory for the control volume.
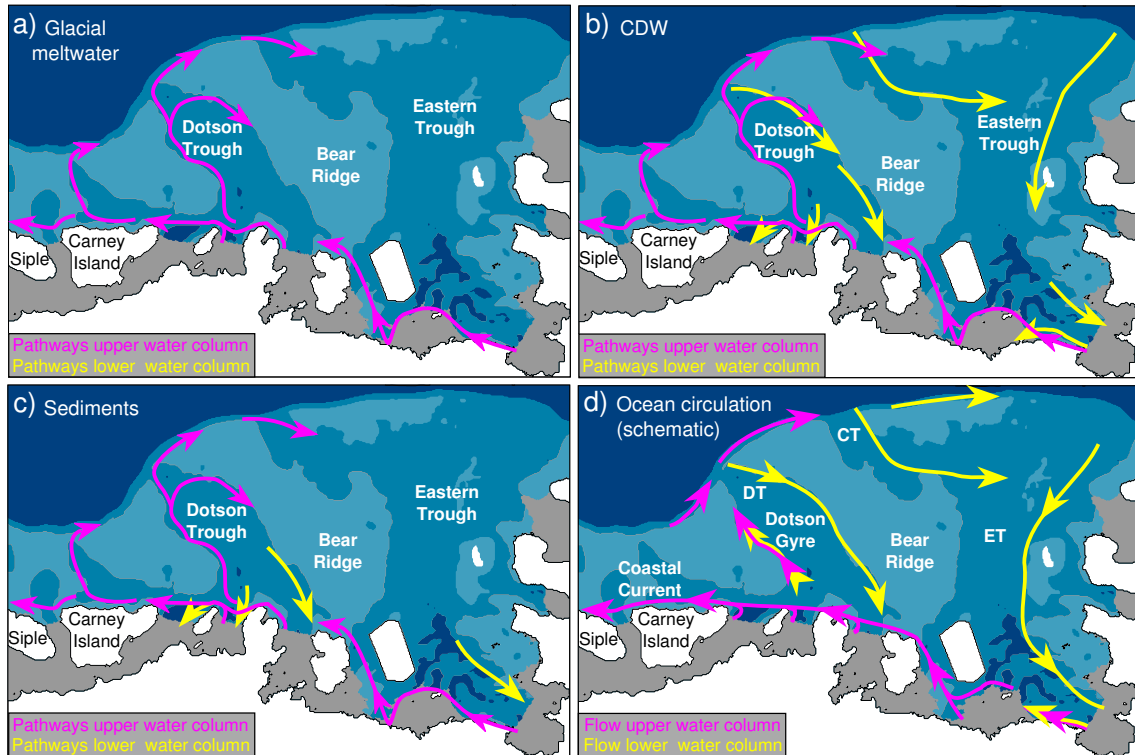
Figure 8. Schematic for the pathways of the tracers representing dissolved iron. (a) Pathways for glacial meltwater. Magenta (yellow) arrows represent approximately the pathways in the upper (lower) half of the water column. A video showing the evolution of the tracer over time is available in 'Supporting Information'. (b) Same but for Circumpolar Deep Water (CDW). (c) Same but for dissolved iron from deep sediments. (d) Schematic for the mean simulated ocean circulation on the continental shelf. DT is Dotson Trough, CT is Central Trough, ET is Eastern Trough.
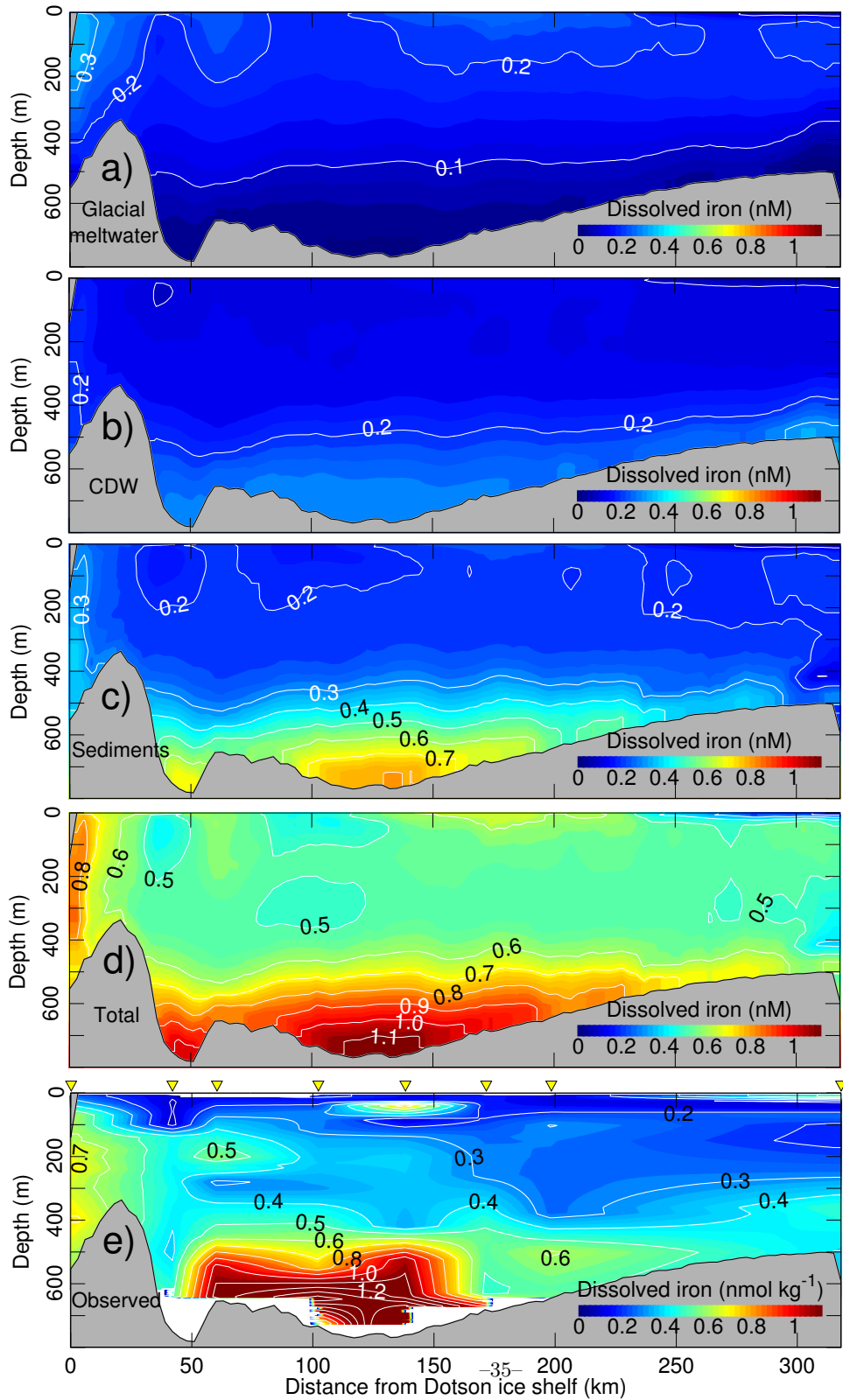
Figure 9. Vertical distribution of dissolved iron from the Dotson ice shelf to the shelf break (see Figure 1 for the location of the section in green). (a) Dissolved iron associated with the glacial meltwater tracer after 13 years of spin-up (average for Dec. 2010). (b) Same as (a) but for the CDW tracer. (c) Same as (a) but for the sediments tracer. (d) Sum of a, b and c. (e) Observed distribution in Dec. 2010 [*Sherrell et al.*, 2015]. Yellow triangles indicate observed profiles (from left to right: Station 60, 57.04, 57.26, 29, 6, 34, 66, 4).
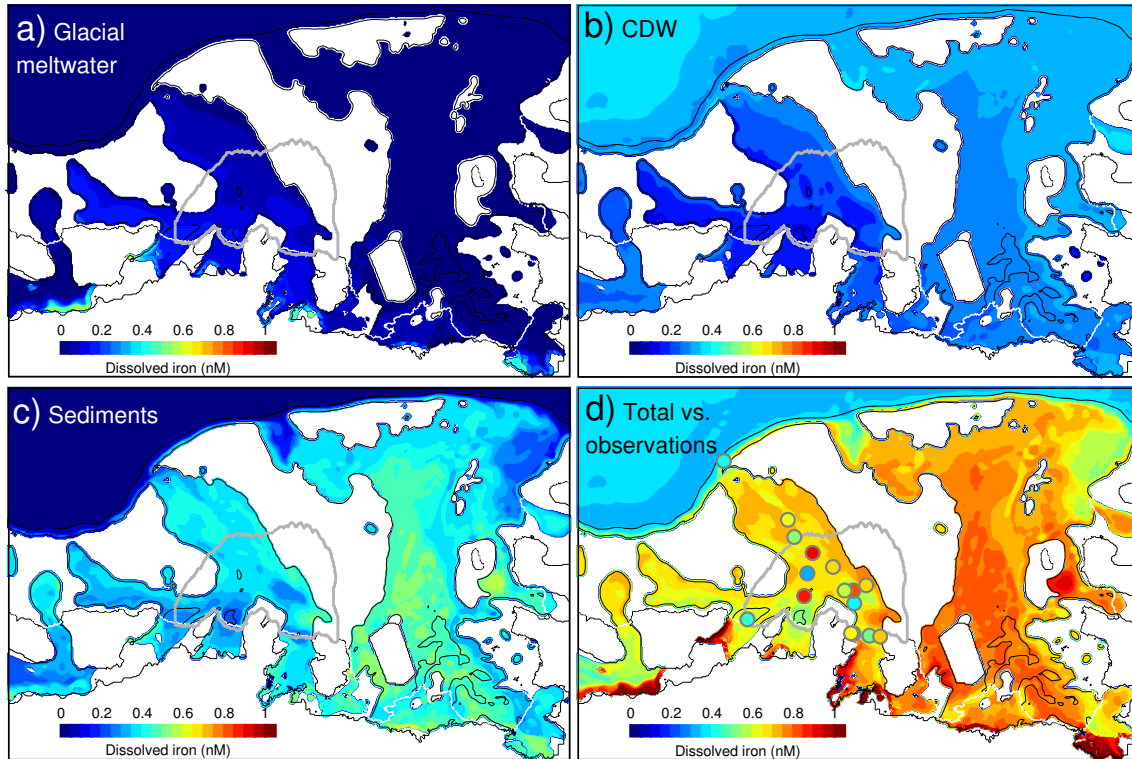
Figure 10. Horizontal distribution of dissolved iron (500 meters depth). (a) Dissolved iron associated with the glacial meltwater tracer in Dec. 2010 (13 years of spin-up). The gray contour line is the control volume (climatological extent of the polynya in January). Black contour lines represent the grounding line and 500 m/1000 m isobaths. The white contour line is the ice shelf front. (b) Same as (a) but for the CDW tracer. (c) Same as (a) but for the sediments tracer. (d) Sum of a, b and c compared to observations (colored circles).
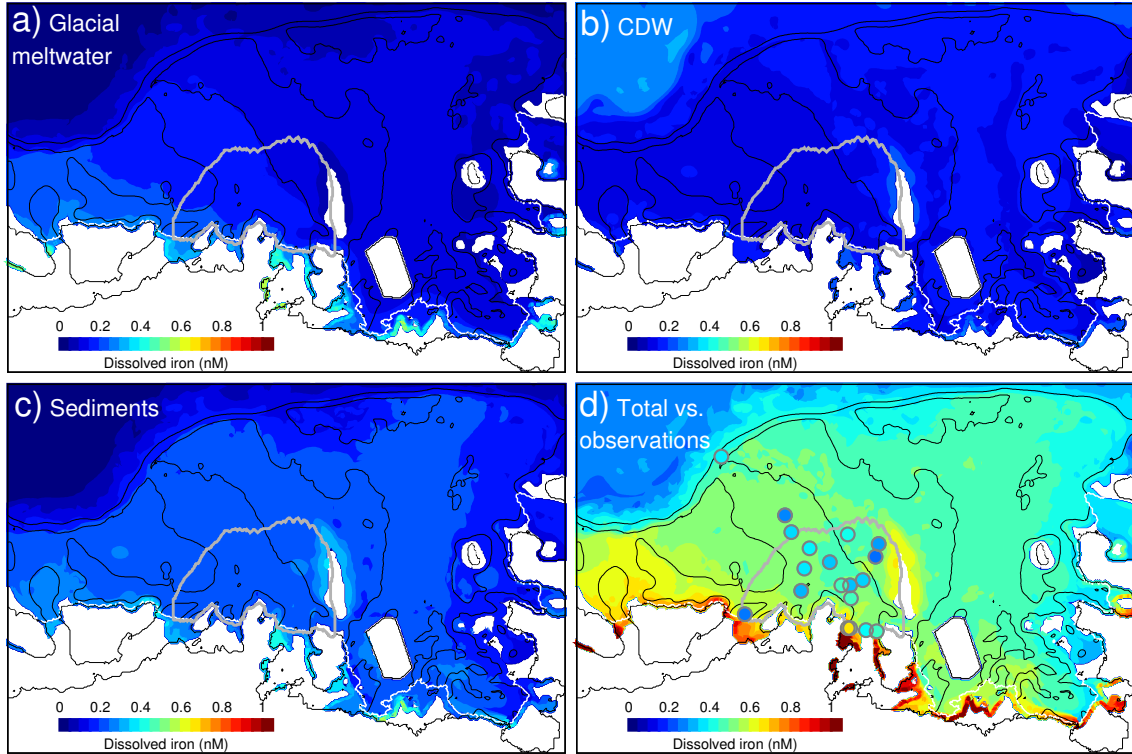
Figure 11. Same as Figure 10 but at 300 meters depth.
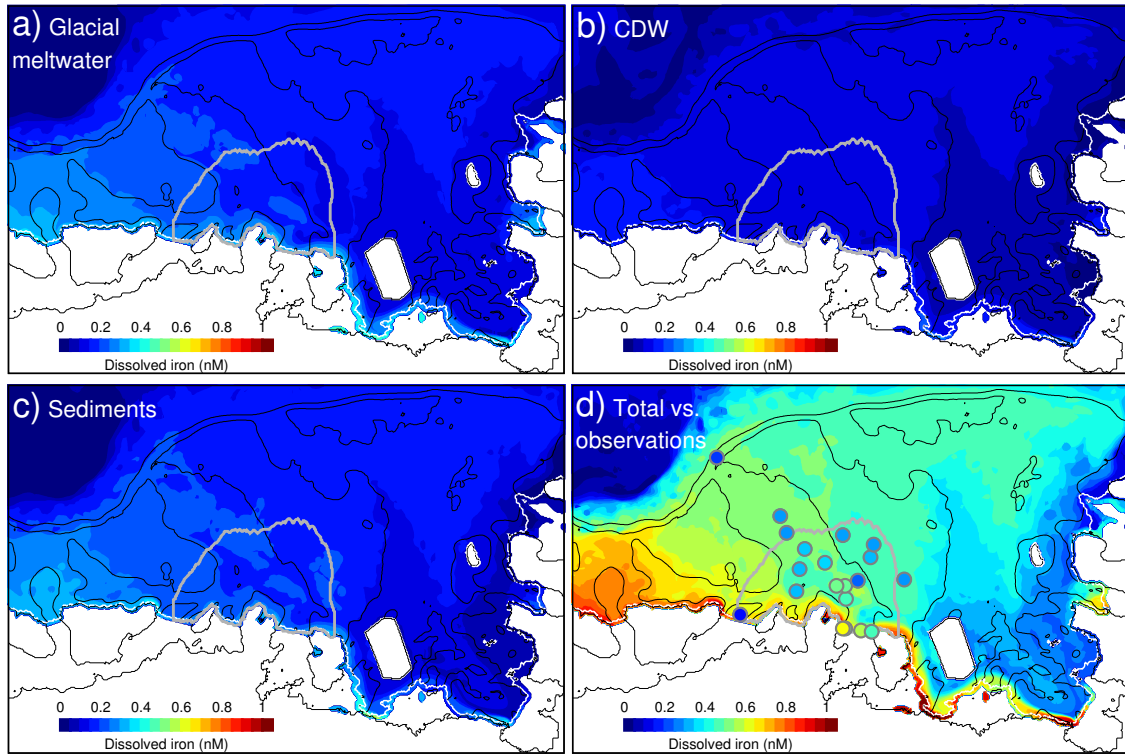
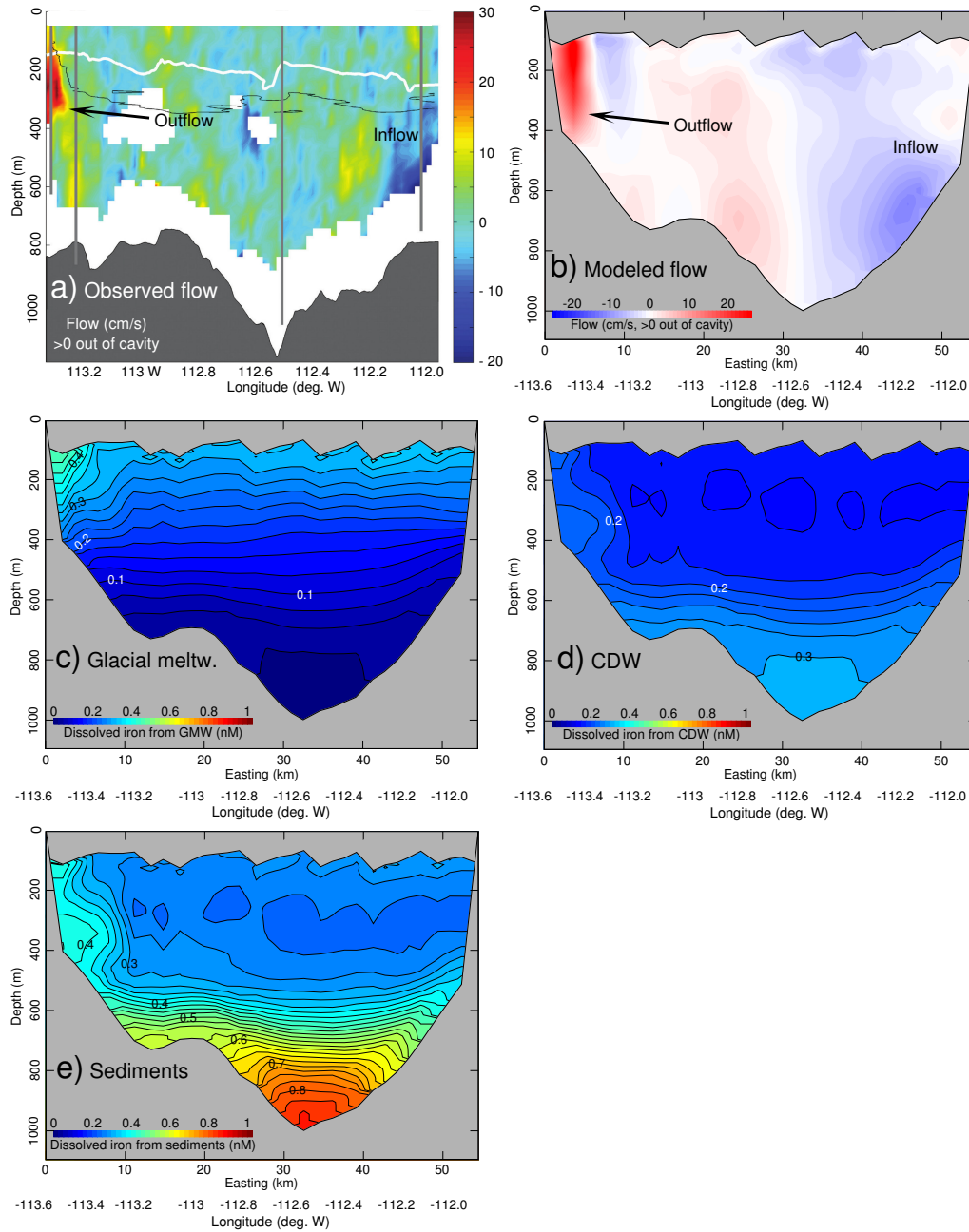**Figure 12.** Same as Figure 10 but at 150 meters depth.

Figure 13. Conditions at the front of the Dotson ice shelf in December 2010 (yellow line in Figure 1). (a) Instantaneous flow observed 200 m offshore of the ice shelf front from underway current-meter data [*Randall-Goodwin et al.*, 2015]. The white line is a multibeam estimate of the ice shelf draft, the black line is the −1°C isotherm, the vertical gray lines indicate sampled stations, and the bathymetry is from *Nitsche et al.* [2007]. (b) Simulated flow along the ice shelf front (grid point closest to ice shelf draft of 100 m). The model results represent an average over the month. (c) Dissolved iron associated with glacial meltwater. The contour interval is 0.025 nM. (d) Same as (c) but for CDW. (e) Same as (c) but for sediments.
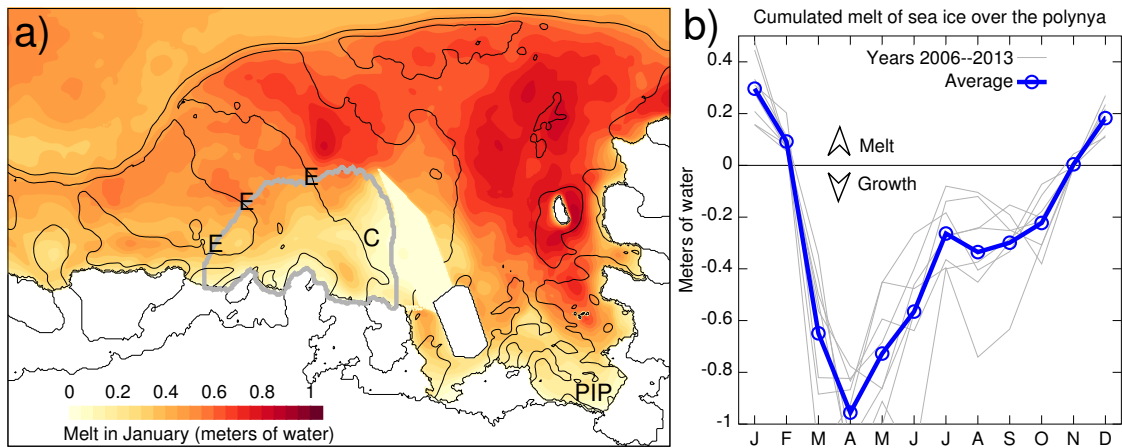
Figure 14. Simulated sea ice melt over the Amundsen Sea. (a) Spatial distribution of cumulated sea ice melt in January (month of maximum melt and maximum biological production; figure is an average over 2006–2013). The gray contour line is the control volume (climatological extent of the polynya in January). Letters 'C' and 'E' represent the Center and Edge of the Amundsen Sea Polynya. PIP is Pine Island Polynya. Black contour lines represent the ice shelf front, grounding line, and 500 m/1000 m isobaths. (b) Monthly cumulated sea ice melt/growth over the control volume. Note that the polynya is a net producer of sea ice (annually-averaged value is negative).
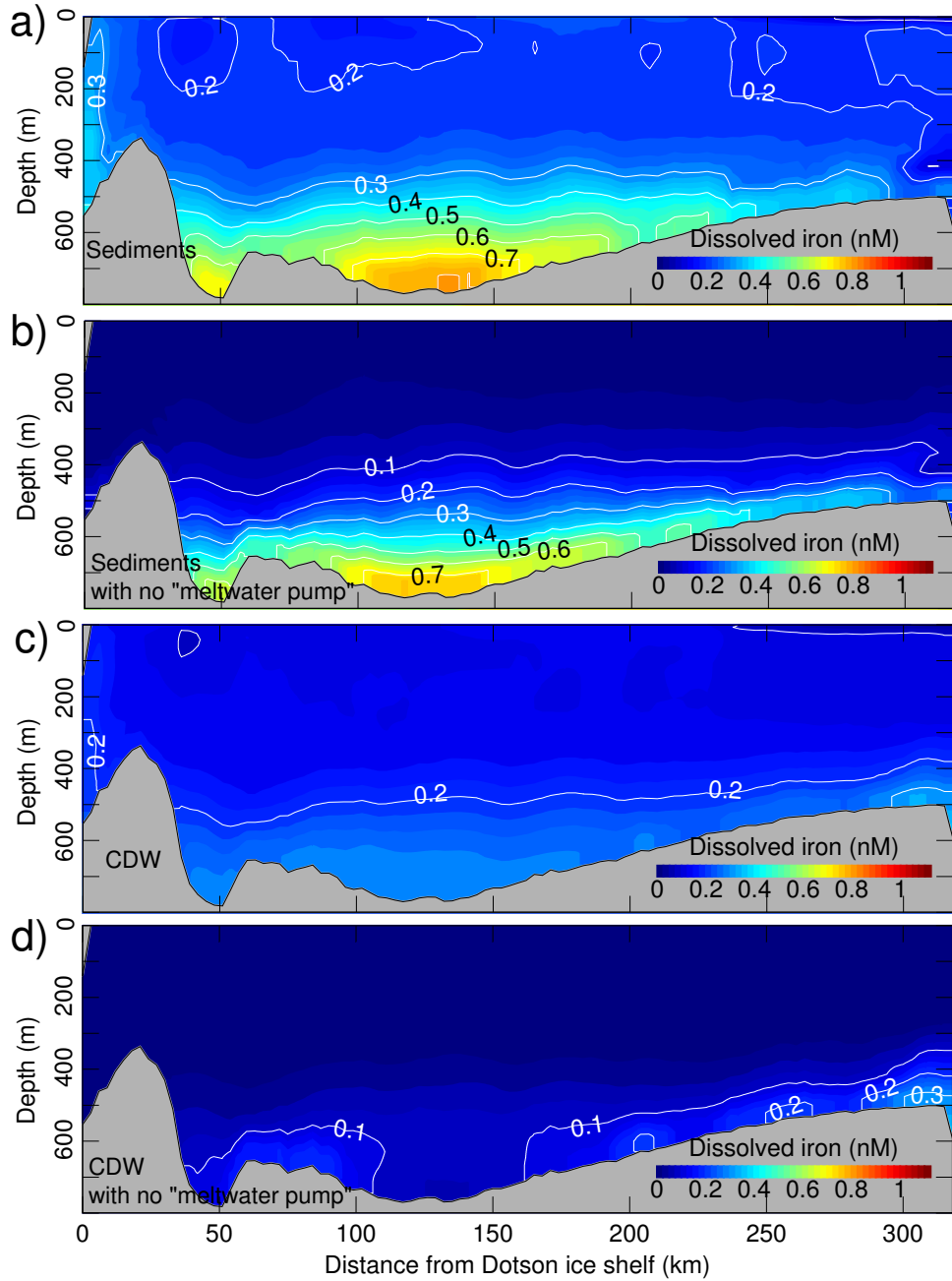
Figure 15. Vertical distribution of the two deep iron sources (CDW, sediments) in cases where the tracer is prevented from exiting the ice shelf cavities. (a) Dissolved iron from sediments. The figure is repeated from Figure 9c for comparative purposes. (b) Dissolved iron from sediments in the case where the tracer is nudged to zero inside the cavities (no meltwater pump). (c) Dissolved iron from CDW. The figure is repeated from Figure 9b for comparative purposes. (d) Same as (b) but for CDW. The tracers represent an average over the month of Dec. 2010 (13 years spin-up).
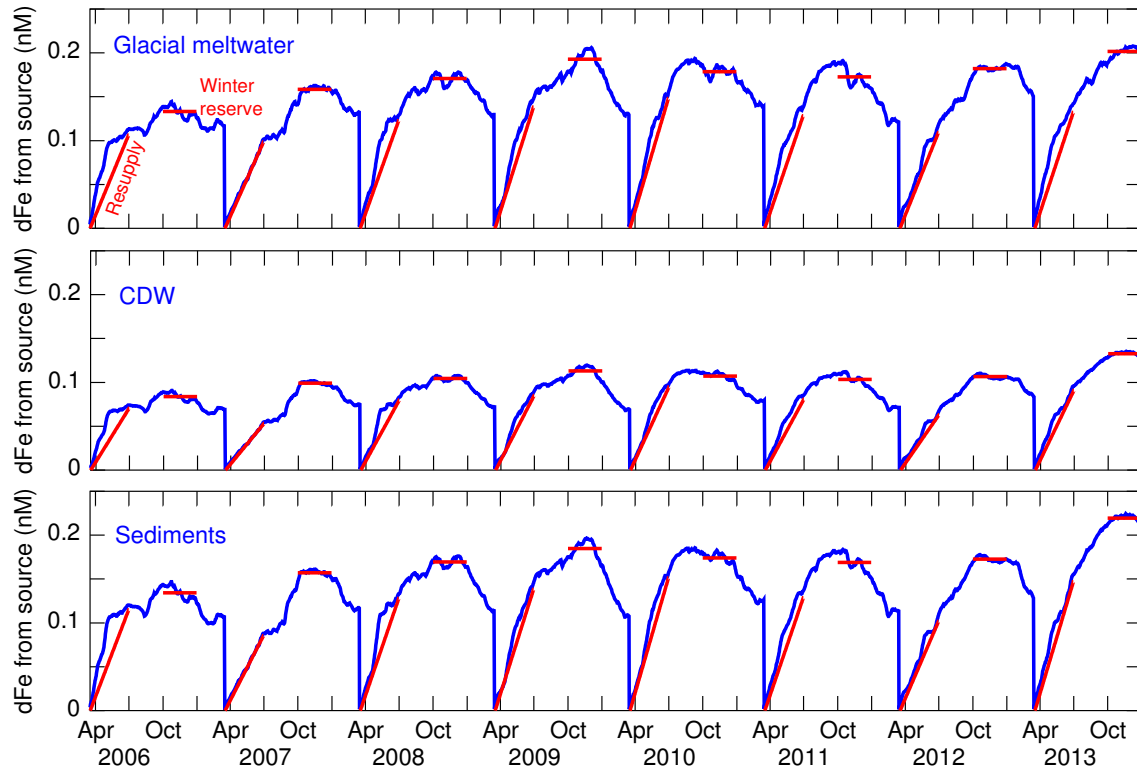
Figure 16. Renewal of the tracers in the control volume (upper 100 m of the polynya) after the idealized drawdown. The timeseries represent the iron from each source averaged over the control volume. The horizontal red line is the pre-bloom inventory (winter reserve) defined as the average concentration between Oct. 1 and Jan. 1. The oblique red line is the rate of replenishment defined as the average slope between March 15 and July 1.

Table 1. Contribution of each dFe source to the inventory of the control volume (upper $100\,\mathrm{m}$ of the polynya) in the experiment with idealized drawdown[a]

Source	End-member nM	Winter reserve[b] nM	Supply rate nM month^{-1}
Glacial ice	20	0.17 ± 0.02[c]	0.036 ± 0.005
Sediments	[d]Fig. 6c	0.17 ± 0.02	0.036 ± 0.007
CDW	0.37	0.13 ± 0.01	0.023 ± 0.004
Sea ice	5	0.03 ± 0.01	Not applicable

[a]See Section 2.4.2 for the definition of the terms.
[b]'Winter reserve' and 'Supply rate' are averaged over 2006–2013.
[c]The $\pm$ is the standard deviation for the 8 annual values.
[d]The sediment source uses a spatially-variable end-member (Fig. 6c).